Quarterly Journal of the Royal Meteorological Society Q. J. R. Meteorol. Soc. 141: 166–181, January 2015 A DOI:10.1002/qj.2347

RMetS
Royal Meteorological Society

Evaluation of the GECCO2 ocean synthesis: transports of volume, heat and freshwater in the Atlantic

Armin Köhl*

Institut für Meereskunde, Zentrum für Meeres- und Klimaforschung, Universität Hamburg, Germany

*Correspondence to: A. Köhl, Institut für Meereskunde, Universität Hamburg, Bundesstrasse 53, 20146 Hamburg, Germany.
E-mail: armin.koehl@zmaw.de

We present results from a new synthesis (GECCO2) which covers the years 1948 to 2011 employing a similar configuration of the Massachusetts Institute of Technology general circulation model as the previous 50-year (1952 to 2001) GECCO synthesis. In GECCO2, the resolution was increased; it now includes the Arctic Ocean and a dynamic/thermodynamic sea ice model. The synthesis uses the adjoint method to bring the model into consistency with available hydrographic and satellite data as well as prior estimates of surface fluxes. In comparison to GECCO, GECCO2 provides a better agreement with the assimilated data, however the estimated flux adjustments remain similar to GECCO. Global heat content changes are in agreement with recent observational estimates and the estimate of the global heat flux is close to a radiative forcing estimate. Both show a clear effect of the radiative forcing from volcanic eruptions and a weak relation to ENSO events. In contrast to GECCO, the importance of the Denmark Strait overflow for the variability of the Atlantic Meridional Overturning Circulation (AMOC) is replaced in GECCO2 by water mass transformation in the subpolar gyre, which is shown to be part of the thermohaline circulation if the overturning is defined as a function of density. Heat and freshwater transport estimates in the Atlantic are more consistent with previous estimates than the unconstrained run. Decomposing heat and freshwater transports into overturning and gyre components by averaging on density coordinates demonstrates that in these coordinates the contribution from the gyre circulation largely disappears for heat transport and is reduced for the freshwater transport.

Key Words: ocean synthesis; heat content changes; freshwater transport; heat transport; Atlantic meridional overturning

Received 16 April 2013; Revised 29 January 2014; Accepted 30 January 2014; Published online in Wiley Online Library 26 March 2014

1. Introduction

Ocean syntheses are based on combinations of model dynamics with sparse observational data to yield a complete description of the changing ocean consistent with the dynamical equations embedded in the ocean model. During the last decade, ocean syntheses have evolved from an experimental endeavour to a standard product conducted by many operational and research centres. In comparison to the first Conference on the Ocean Observing System for Climate OceanObs'99, the role of ocean syntheses in OceanObs'09 was much more visible. This demonstrates how much ocean data assimilation is nowadays an integral part of observing the ocean.

While the period before 1999 was mainly devoted to the development and testing of assimilation methods, in the recent decade many (more than 30) quasi-operational products routinely synthesize various observations with global models over periods of several decades (e.g. Balmaseda *et al.*, 2010; Heimbach *et al.*, 2010; Lee *et al.*, 2010b; Stammer *et al.*, 2010; Xue *et al.*, 2010) and many of them are easily available for download (http://icdc.zmaw.de/easy_init_ocean.html). However, despite the large number of products which were successfully evaluated, intercomparisons among different products still reveal a mixed picture since some aspects appear to be consistent across the products while others disagree (e.g. Carton and Santorelli, 2008; Lee *et al.*, 2010a; Munoz *et al.*, 2011, and references above).

At the beginning, ocean syntheses were primarily designed for ocean (e.g Bahurel, 2006) and seasonal prediction (e.g. Goddard *et al.*, 2001) and for describing the ocean state (e.g Stammer *et al.*, 2002). With the upcoming interest in decadal climate predictions (e.g. Smith *et al.*, 2007; Keenlyside *et al.*, 2008; Pohlmann *et al.*, 2009), the focus of has now shifted toward their use for initialization of decadal climate predictions (Balmaseda *et al.*, 2010) and for the description of climate variability (e.g. Köhl and Stammer, 2008a, 2008b).

Among the wide range of existing methods of assimilating data into global ocean models, only the coupled data assimilation system K7 (Sugiura *et al.*, 2008) and the Estimating the Circulation

and Climate of the Ocean system (ECCO; Wunsch and Heimbach, 2006; Köhl *et al.*, 2007) are based on the adjoint method, which allows for a description of the ocean circulation that obeys exactly the dynamical principles as formulated by the model equations. In comparison to sequential methods, the advantage is a more straightforward interpretation of changes, but the risk might be that the estimated state may be more impaired by imperfections of the model.

In the following, we will evaluate an update of the GECCO (German contribution to ECCO) synthesis (Köhl and Stammer, 2008a, 2008b) that is based on a new configuration of the ocean model featuring higher horizontal and vertical resolution and additional physics. We will investigate the mean meridional overturning in the Atlantic and revisit the causes for its changes. In the Atlantic, transports of heat and freshwater are compared to GECCO and independent estimates. A new aspect is an analysis on density surfaces of transports of volume, heat and freshwater. After introducing the synthesis in section 2, the focus of section 3 will be on the evaluation with mainly, although not exclusively, the assimilated data. Section 4 evaluates the estimated state against independent estimates with foci on heat content changes, meridional overturning, and heat and freshwater transports.

2. Methods

The syntheses described here (GECCO2 in the following) covers the years of the National Centers for Environmental Prediction (NCEP) RA1 reanalysis 1948–2011 with the intention of producing annual updates to facilitate initialization of decadal predictions. GECCO2 is based on a similar configuration of the Massachusetts Institute of Technology general circulation model (Marshall *et al.*, 1997) as GECCO. Zonally, the resolution is 1° as for GECCO, but GECCO2 uses higher vertical resolution (50 levels versus 23 levels) and a meridional refinement to 1/3° at the Equator, plus approximately isotropic cells between 20° and 60°, identical to the shorter synthesis of Köhl *et al.* (2012), which covered only the years 2002–2007. As an additional improvement to GECCO, GECCO2 now includes the Arctic Ocean with roughly 40 km resolution and the dynamic/thermodynamic sea ice model of Zhang and Rothrock (2000). The bathymetry is essentially the same as Köhl *et al.* (2012); only the sill depth of the Strait of Gibraltar is reduced to 240 m to reduce the too large exchange with the Mediterranean.

The synthesis uses the adjoint method to bring the model into consistency with available hydrographic and satellite data, including the prior estimate of the atmospheric state by adjusting the control vector. Apart from the initial conditions for temperature and salinity, the control vector includes the atmospheric state on the model grid every 10 days, which is linearly interpolated to the model time and which includes surface air temperature, humidity, precipitation and the 10 m wind speeds. Surface fluxes are derived by the model via bulk formulae according to Large and Pond (1981, 1982) with the updated function of bulk transfer coefficients after Large and Yaeger (2004), and freshwater forcing is represented by a virtual salt flux. The prior of the atmospheric state derives from the 6-hourly NCEP data and the set of assimilated data includes along-track altimeter data from Topex/Jason (TP), ERS1/ERS2/Envisat (ERS) and the Geosat Follow-On mission (GFO), Advanced Microwave Scanning Radiometer (AMSR/E) and the Hadley Centre Global Sea Ice and Sea Surface Temperature (HadISST) dataset. As the model employs the Boussinesq approximation, its global mean sea level is constant. Therefore, the global mean estimated from mapped altimeter data was subtracted from the along-track altimeter data. Temperature and salinity profiles taken from the EN3 v2a database (Ingleby and Huddleston, 2007) are quality controlled and bias corrected according to the processing of Wijffels *et al.* (2008). Additionally, the mean sea-surface height from the combination of the Gravity Observation Combination (GOCO02) geoid (Pail *et al.*, 2010) with the Centre National d'Études Spatiales (CNES) CLS11 mean sea surface and climatological temperature and salinity from the World Ocean Atlas 2009 (WOA09; Levitus *et al.*, 2009) are assimilated. The WOA09 product applied a drop-rate correction to the expendable bathythermograph (XBT) data.

Error weights are specified as in Köhl *et al.* (2012) and are dominated by the representation error of the model due to unresolved eddies. For the atmospheric state, errors are calculated as before from the STD of the NCEP fields. Modifications to the adjoint are necessary because of the nonlinearity of the model and are as described in Köhl and Stammer (2008b). For the mean dynamic topography and the climatological temperature and salinity fields, a constant of 4.5 cm and vertical profiles as in Köhl and Stammer (2008b) were used, respectively. Note that the error of the *in situ* data contains the representation error, which, in regions with strong mesoscale variability, can be up to a factor of 10 larger than the profile used to constrain the climatological data. However, since the climatology is used only to constrain the mean, its effect on every monthly mean is effectively a factor of 60 smaller.

We describe here two runs, which were both started on 1 January 1948 from one year of spin-up after initializing from rest, with temperature and salinity conditions taken from the January fields of WOA09. CTRL is based on the same model configuration as GECCO2 and is forced with the 6-hourly atmospheric state from NCEP RA1 employing additionally surface relaxation with a time-scale of 30 days to HadISST and climatological salinity values. GECCO2 is the synthesis as described above and we analyze here the state after 23 iterations. During the course of iteration, a few changes had to be introduced to the set-up which should be explained here. The optimization procedure was started as a synthesis over the period 1948–2009 until iteration 9, beyond which no further reduction was achievable. Since at that stage regional surface salinity differences to the climatology of up to $2\,\mathrm{g\,kg^{-1}}$ remained, climatological salinity was additionally assimilated as monthly sea-surface salinity (SSS) during the following iterations, which further reduced the model–data differences of all data until iteration 14, where the progress stalled.

For the following iterations that covered the complete period 1948–2011, the strategy was changed again and the period was partitioned into five-year segments that include one year overlap at the end of each part, similar to the strategy of Sugiura *et al.* (2008). The initial integration of the adjoint over the complete period enables information from the later decades to affect earlier decades, while the integrations over shorter periods afterwards is able to better cope with the nonlinearity of the model, which may cause multiple cost function minima, whose number is likely to increase with the length of the integration. As for the previous iterations, only the initial conditions of year 1948 were included in the control vector, and for the subsequent periods the conditions at the end of year 4 of the previous part served as initial conditions. Therefore, no artificial sources or sinks of heat, freshwater and momentum were added throughout the integration. Iterations were performed on each part separately before moving to the next part. To compensate for the larger weight of the climatology in the individual parts, the weight was reduced by a factor of 10, and the mean sea level was re-referenced for each period after 1992 with the AVISO sea-level anomaly maps.

3. Evaluation with assimilated data

The success of an assimilation can be objectively assessed with the cost function contributions. For consistency of the model with the data and the prior errors, the RMS difference of the solution from the data should be close to the prior error estimates, which is achieved if the normalized averaged RMS differences are close to one. Figure 1 shows that, for most of the contributions, values range between 1 and 2, while for the *in situ* temperature and salinity profiles, values ranges between 2 and 3. The failure to meet

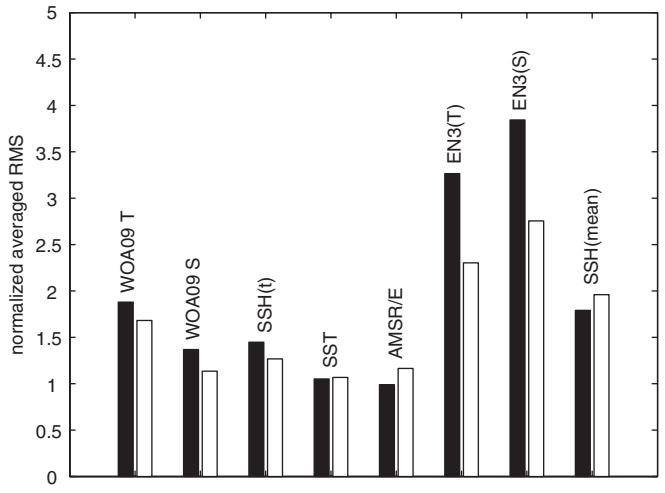

Figure 1. Global and time-mean RMS difference from different observational datasets as indicated by the labels for CTRL (black) and GECCO2 (white). Values are normalized by the model–data error and a value of one is required for consistency with the prior error estimate.

the requirement for consistency is not surprising since the prior error estimate was based only on measurement and representation errors due to unresolved mesoscale eddies, while the model cannot be regarded as otherwise perfect, and deficiencies cannot be solely represented as corrections to the atmospheric state. However, in comparison to the cost function values of GECCO (Köhl *et al.*, 2006), most contributions are reduced. Values for SST and the mean sea level are slightly smaller, and the contribution of sea-level anomalies reduced from 1.6 to 1.3.* It should be noted that the unconstrained run is much improved in all aspects compared with the previous control. Despite the fact that both CTRL and the corresponding run of the previous solution employ a 30-day relaxation to SST, only the new run, forced with the atmospheric state, achieves a consistent SST, while previously, when forced with fluxes, the RMS error was about a factor of 3 larger. Therefore, improvements are clearly related to the change in the set-up of the forward model.

Mean adjustments to the fluxes which were estimated in order to bring the model into consistency with the data are shown in Figure 2. Note that these fluxes were not the direct control variables but emerge diagnostically from the changes to the atmospheric state and the displayed correction to the fluxes are calculated as difference from those of CTRL. In comparison to GECCO (Köhl *et al.*, 2006), the heat flux corrections of GECCO2 are of about equal strength and show similar patterns, particularly near the western boundary current systems. A noticeable difference are the stronger positive values in the North Pacific between 10°N and 30°N. Freshwater flux corrections are nearly identical to GECCO. However, differences are noticeable near the ice edge and near river mouths. While some of the corrections of GECCO mimic the missing ice model, the corrections in GECCO2 are mainly a consequence of changes in the state of the ice model, rather than directly due to changes of the freshwater fluxes. Modifications to the runoff are much less an issue in GECCO2. While corrections to the zonal wind stress remain very similar in the Northern Hemisphere (except for the Bering Sea), in the Southern Hemisphere the uniform band of enhanced westerly wind south of the Subantarctic Front is quite different from GECCO.

The RMS difference from the EN3 temperature profiles drops for CTRL from more than 2 °C in the upper 250 m to less than 0.5 °C below 1500 m (Figure 3). Note that Figure 3 and the following are biased towards the data-rich Argo period, particularly for salinity. The reduction for GECCO is about 0.6 °C above 1200 m. In particular, the large bias up to 1 °C in the upper 500 m disappeared in GECCO2 while further changes below are smaller. For salinity, the largest changes appear between 250 and 1250 m, where the RMS is reduced by about 0.1 g kg^{-1}. The near-surface and deep ocean values remain similar. Unlike temperature, the RMS difference of salinity does not become smaller towards the surface in the upper 100 m. It is most likely the complete good-quality SST data that helps to adjust the heat fluxes no matter whether assimilated or being just part of a relaxation term, while for both cases the climatological SSS does not provide sufficient information for the time-varying SSS signal. However, as noted in section 2, due to the sparsity of the salinity data, even climatological SSS is an essential piece of information, without which the reduction of subsurface salinity differences remains much lower.

Compared with GECCO, GECCO2 shows substantially smaller RMS temperature differences in the range 250–1000 m. However, below 2250 m this observation reverses and GECCO shows smaller RMS differences. The origin of the larger difference in GECCO2 lies in the northern North Atlantic where higher (by up to 1 °C) temperatures exist in the deep western boundary current (DWBC). For salinity, GECCO2 and GECCO perform similarly. Although GECCO ends with year 2001 and misses the data-rich Argo period completely, the influence of different periods on the GECCO2 curves is quite small and leads, particularly for salinity, to nearly identical results. In comparison to the Operational Ocean Reanalysis System (ORAS4; Balmaseda *et al.*, 2013a), which is based on a sequential assimilation method which allows for the correction of model biases, the RMS differences are in the same range. Differences to temperature observations are only slightly higher (a maximum of 2 °C in comparison to 1.75 °C) yet lower for salinity (a maximum of 0.6 in comparison to 0.8).

The temporal evolution of the RMS differences is shown in Figure 4. Apart from some outliers due to insufficient quality control, a clear maximum below 1000 m, which builds up during the first 20 years, is noticeable. Within the Argo period, this signal becomes very smooth and well defined. A horizontal map at 1000 m (not shown) shows the signature of a too strong Mediterranean outflow which gets stratified into the North Atlantic at too shallow a depth. After 2005, in the range below 2000 m a signal appears which was weaker and only sporadic before. The range below 2000 m belongs to moorings or conductivity, temperature, depth sensors (CTDs) in the Labrador Sea and the reason why this signal appears after 2005 is the dramatic reduction in number of other CTD stations, most likely owing to the delay with which they get entered into the databases. Therefore, observations predominantly come from moorings, which are located in the DWBC that is not well resolved by the model. In the upper ocean, roughly above 700 m, the RMS differences for temperature and salinity are reduced after the introduction of the Argo data. There can be many reasons for this improvement: the climatology is biased towards the later years and may therefore be more consistent with the ocean state during these years than earlier; Argo sampling is more uniform, while XBTs are sampled more densely in the western boundary current regions where eddy variability produces large RMS differences; finally, more complete information due to the simultaneously sampled salinity data reduces the effect of water mass errors and will provide physically more consistent states.

Regional patterns of temperature and salinity biases and RMS differences are shown at 200 m in Figure 5, although near-surface values are larger for salinity. Apart from the signature of the eddy-rich regions, several areas associated with the North and South Equatorial current systems show large biases and RMS errors. These areas account for a large part of the error reduction, while a large fraction of the reduction in bias appears to be more uniform. A particularly large improvement is visible along 40°S in the Indian and Pacific Ocean where errors of 2 °C and more are reduced to less than 1 °C. In this area, temperature and salinity

*Note that the previously reported value of 0.6 should read 1.6 due to an error in the number of data.

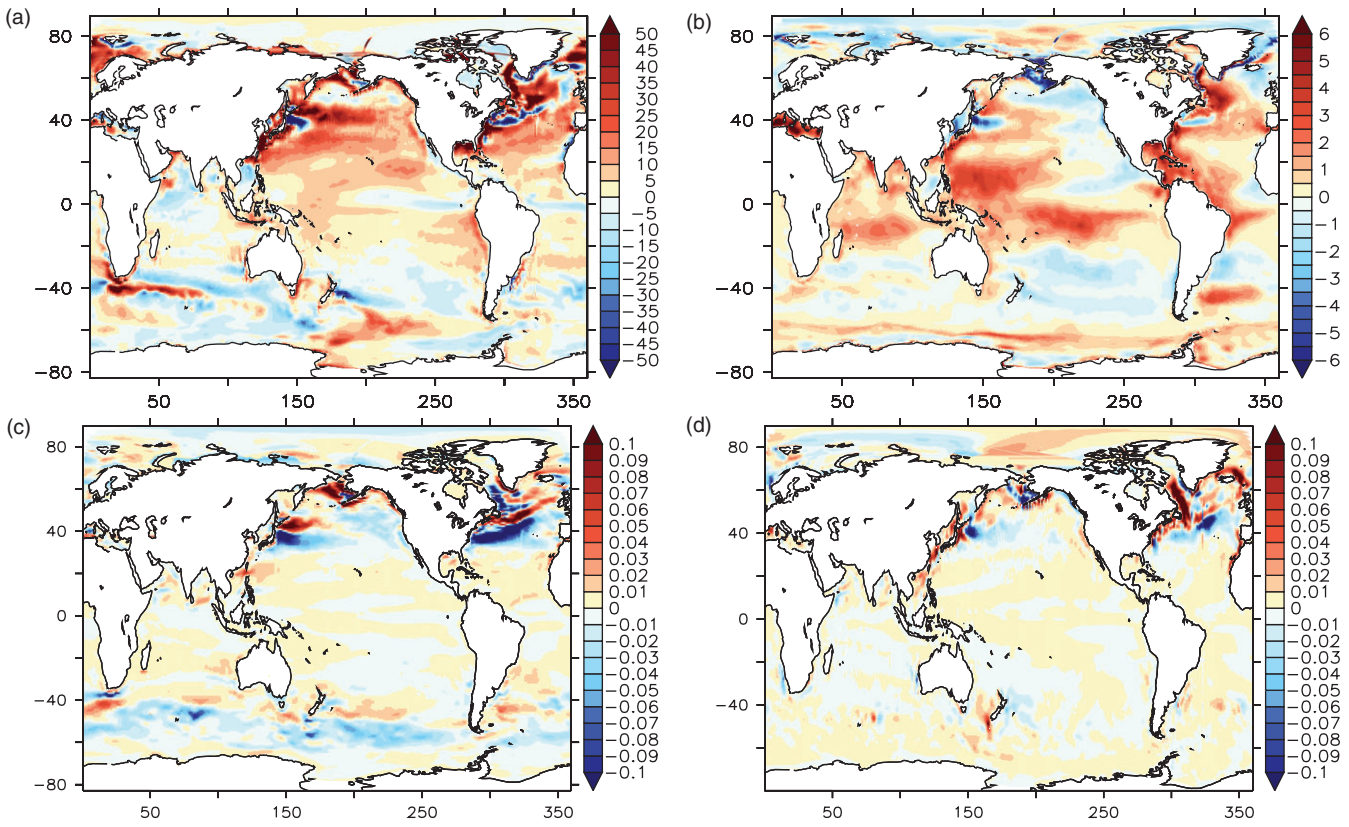

Figure 2. Corrections to (a) the heat ($W\,m^{-2}$), (b) freshwater ($mm\,day^{-1}$), (c) zonal and (d) meridional wind stress ($N\,m^{-2}$). The sign of the fluxes follow the NCEP convention with positive values into the atmosphere.

biases have the same sign, such that the impact on density and the current structure remains small. It is therefore an error in spiciness of the Subantarctic Mode Water, which is formed in the Subantarctic region where Subantarctic Water competes with southward flowing warmer saltier water from western boundary current extensions. The northward Ekman transport, associated with the westerly winds, is suggested as being important for shaping the characteristics of these water masses (Rintoul and England, 2002). The clear strengthening of the westerly winds south of the Subantarctic Front (Figure 2), which enhances the contribution from the cold and fresh Subantarctic Water, suggests that this is also how the warm and salty bias was removed in GECCO2.

The RMS differences from the along-track TOPEX/Poseidon sea-level anomalies demonstrate that the largest differences are related to the eddy-rich regions, which are not reduced (not shown). Therefore, we show in Figure 6 the RMS difference normalized by the STD from the model and the data. Reductions are visible mainly in regions of lower variability between 40°S and 30°N , particularly in the Tropics where wind-forced variability dominates the eddy variability. However, an increase in error is observable in the North Atlantic and the northern North Pacific. In these regions, the interannual variability is higher in GECCO2 than the altimeter data and shows low correlation while CTRL has lower variability than the data with good correlation in the North Pacific. Globally, GECCO2 shows higher variability than CTRL, but still too low variability compared with the altimeter data on monthly time-scales (not shown). On interannual time-scales, the level of variability of GECCO2 matches the data well (Köhl, 2014).

4. The estimated state

In the following, several measures for the time-mean and variable ocean circulation and its response to climate change are analyzed. We will focus here on quantities that are observed or for which results from other studies are available.

4.1. *Global heat content changes*

The estimation of the global 60°S–60°N mean heat content changes has already accumulated some history, even though it started only little more than 10 years ago when Levitus *et al.* (2000) reported a warming trend. After several updates (e.g. Levitus *et al.*, 2005a, 2005b), it became clear that instrumental biases severely impact the details of how the ocean responds to changes of the Earth's heat balance due to instrumental offsets and problems with the estimation of the fall rate (Gouretski and Koltermann, 2007). Additional corrections methods were proposed (e.g. Wijffels *et al.*, 2008; Ishii and Kimoto, 2009; Gouretski and Reseghetti, 2010). To date, the three most recent estimates of the ocean heat content (OHC) changes in the 0–700 m layer (Domingues *et al.*, 2008; Levitus *et al.*, 2009; Ishii and Kimoto, 2009) now show a similar trend, but differ still in their interannual variability (Levitus *et al.*, 2009). We show in Figure 7 a comparison of results from GECCO2 and CTRL with the latter two estimates. GECCO2 and CTRL yield similar curves which compare slightly better with Levitus *et al.* (2009) than with Ishii and Kimoto (2009) in terms of overall trend and interannual variability. Compared with Ishii and Kimoto (2009), a pronounced minimum at the end of the 1960s and the smaller maximum at the beginning of the 1980s and 1990 are noteworthy.

The associated global mean heat flux as it results from the NCEP atmospheric state shown in Figure 2 reveals a large offset for CTRL of about $4\,W\,m^{-2}$, which was corrected by the relaxation to HadISST. Aside from the offset, the interannual variability remains relatively similar to GECCO2 ($r = 0.64$). The overall trend in GECCO2 and the three largest minima related to volcanic eruptions compare well to the radiation based estimate by Murphy *et al.* (2009) (the correspondence to CTRL is weaker). A weak relation to the Niño 3.4 index ($r = 0.37$ with the index leading by 4 months) exist if the 4-year periods following the volcanic eruptions in 1963, 1982 and 1991 are disregarded. The loss of ocean heat during El Niño years is consistent with Roemmich and Gilson (2011). Note the heat flux estimate of GECCO2 stays below the radiation-based estimate by about $0.5\,W\,m^{-2}$

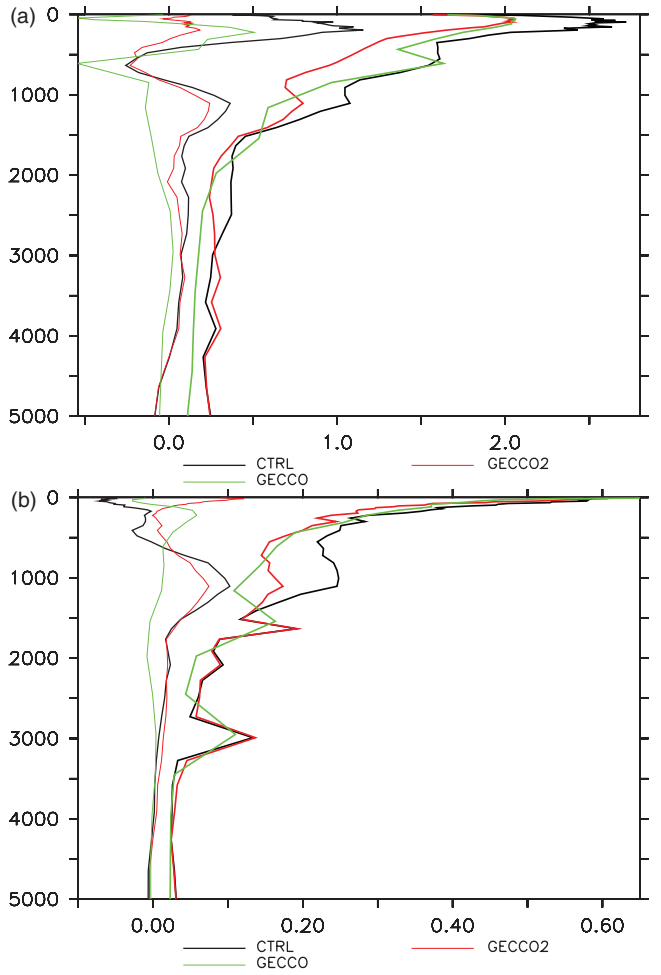

Figure 3. Profiles of bias (thin lines) and RMS difference (bold lines) between the EN3 data and CTRL (black), GECCO2 (red) or GECCO (green) for (a) temperature and (b) salinity.

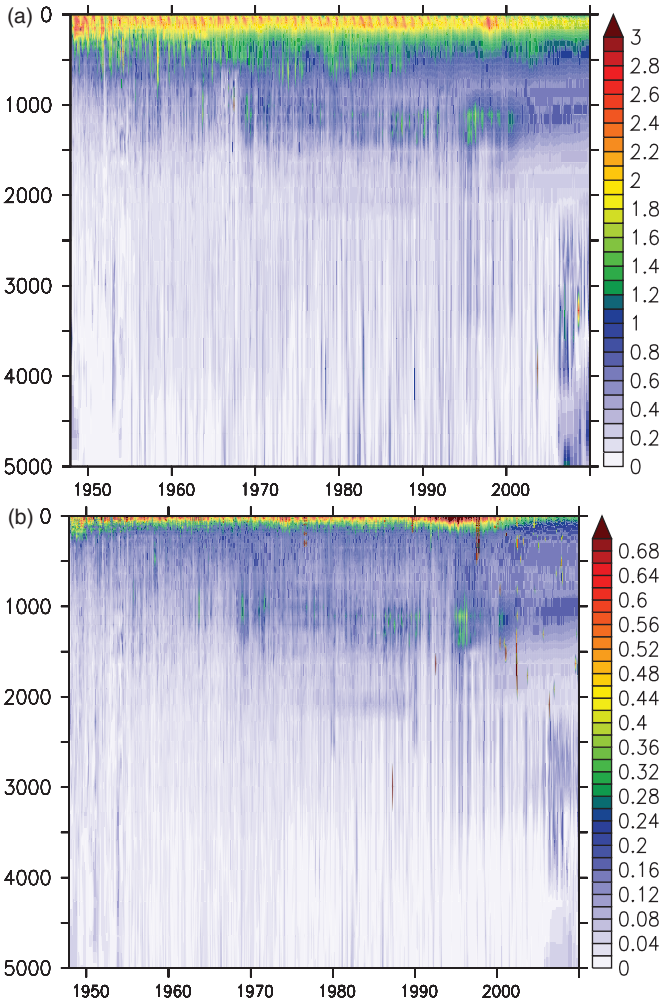

Figure 4. Time series of the RMS difference between the EN3 data and GECCO2 for (a) horizontally averaged temperature and (b) salinity, calculated over the period 1950–2011.

and therefore shows negative values in the period until about 1970. The corresponding decline in heat content is not visible in the layer 0–700 m shown in Figure 7 and takes place in the layers below 700 m (in the tropical Indian and Pacific Ocean), for which the heat content is declining during the first 20 years. We consider this as an artifact due to model drift, which is larger at the beginning and also less constrained by the available data below 700 m during the early years in comparison to the later years. For the more recent decades, the decline becomes close to zero. By contrast, Levitus *et al.* (2012) estimated that about 30% of the warming has occurred below 700 m.

Compared with temperature data, a much lower amount of salinity data is assimilated. However, the global averages of the freshwater fluxes from GECCO2 and CTRL have little in common. After assimilation, a mean bias of $-3.1\,\mathrm{cm\,yr^{-1}}$ remains, compared to values of more than $10\,\mathrm{cm\,yr^{-1}}$ in CTRL, which are balanced by the relaxation to climatological surface salinity. Accumulated over the entire period, the resultant freshwater flux of GECCO2 is -2 m in total. With a mean water depth of about 4000 m, the salinity would change by about $0.03\,\mathrm{g\,kg^{-1}}$, which is consistent with the bias of up to $0.1\,\mathrm{g\,kg^{-1}}$ shown in Figure 3. While CTRL shows more long-term and decadal variability, GECCO2 reveals little long-term change but a quite regular variability on a 4-year time-scale. Although there exists some correlation to the Niño 3.4 index during the 1960s and 1970s, there seems to be no relation in other periods. Since peaks coincide with the years in which individual assimilation windows were initialized, the 4-year signal is likely to be related to details of the assimilation method. The adjoint method fits the data best at the centre of the window, therefore larger deviations from the data and smaller corrections to the freshwater fluxes are expected at the beginning and the end of the window, which leads to 4-year cycles.

4.2. *Atlantic meridional overturning and RAPID measurements*

The meridional overturning circulation in the Atlantic is part of the global thermohaline circulation and characterized by large density conversion. Although often associated just with water mass formation regions in the North Atlantic, the density is controlled by a variety of processes, which include the horizontal gyre circulation (Kuhlbrodt *et al.*, 2007). The importance of the gyre circulation for the Atlantic meridional overturning circulation (AMOC) is a long-recognized fact. Manifold in its influences, its role is ambiguous. The relevance of strength of the subpolar gyre for preconditioning convection has been long known (e.g Marshall and Schott, 1999) and the importance of the gyre transport of heat and salt for the deep convection and the AMOC was shown by e.g. Delworth *et al.* (1993). Dong and Sutton (2005) demonstrated the interactive relation between gyre and AMOC strength as the AMOC also influences the strength of the subpolar gyre. Schematics of the global thermohaline circulation (e.g. McCarthy, 2001) already motivate that in the subpolar North Atlantic, the thermohaline circulation encompasses the overturning as well as the gyre component. As the DWBC off Labrador is shared between the gyre circulation and the AMOC, Böning *et al.* (2006) concluded their direct correspondence and suggested a potential for monitoring the AMOC via sea-surface height data.

However, Zhang *et al.* (2008) claims that AMOC variations are in an out-of-phase relation with the subpolar gyre strength

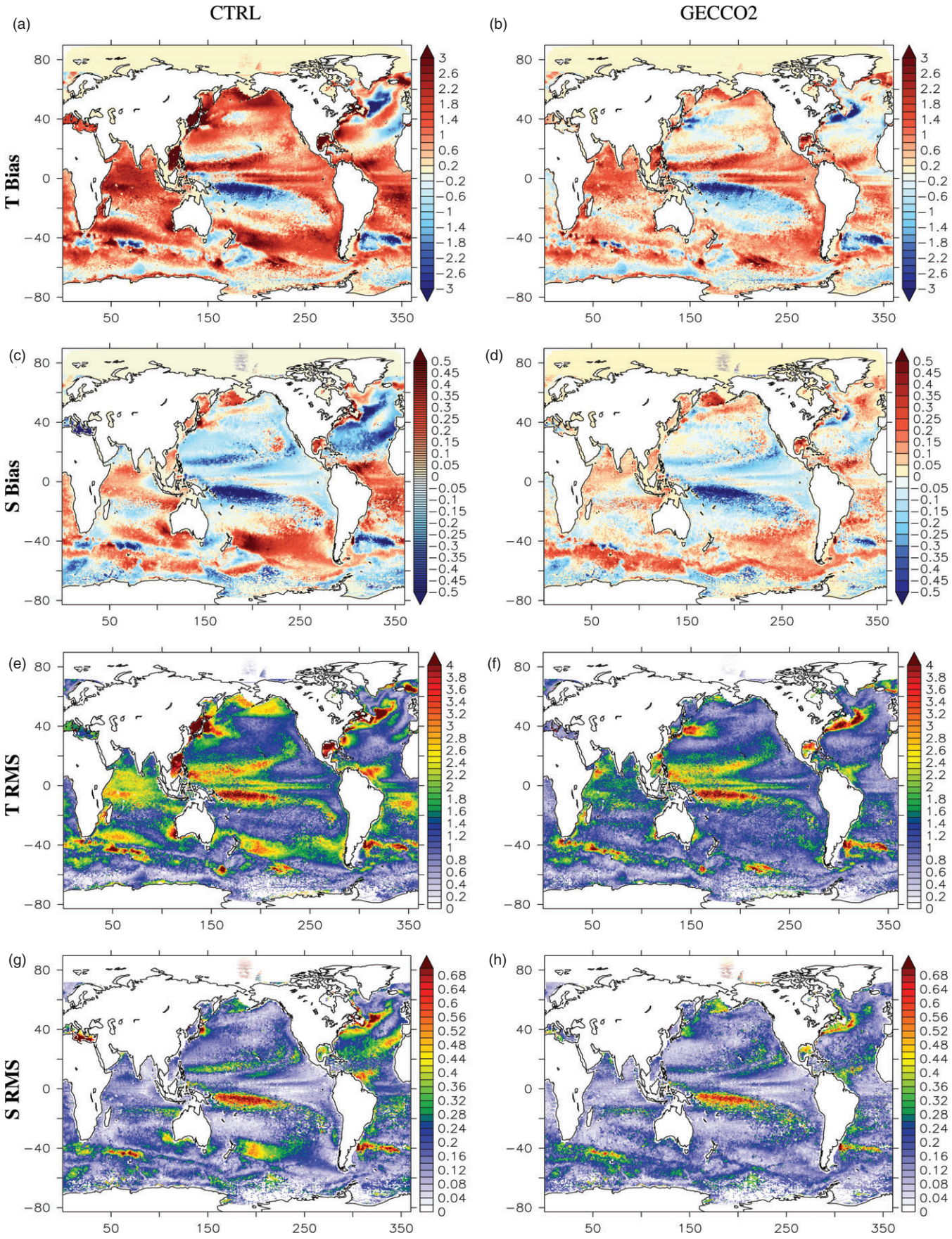

Figure 5. (a)–(d) Bias and (e)–(i) RMS difference at 200 m with respect to the EN3 data for (a, b, e, f) temperature (° C) and (c, d, h, i) salinity ($g\,kg^{-1}$) calculated over the period 1950–2011 for (a, c, e, h) CTRL and (b, d, f, i) GECCO2.

and Eden and Willebrand (2001) demonstrated that the response of the gyre and AMOC to the buoyancy and wind stress forcing components of the North Atlantic Oscillation (NAO) show lag-dependent in-phase as well as out-of-phase relations. We will investigate the role of the subpolar gyre for the AMOC by an analysis in isobaric as well as in density coordinates. The latter provide a natural link of the gyre circulation to the AMOC variability, as the density conversion in the subpolar gyre shows up as overturning as a function of density. This is the complementary effect to the Deacon Cell (e.g. Bryan, 1993) in the Southern Ocean,

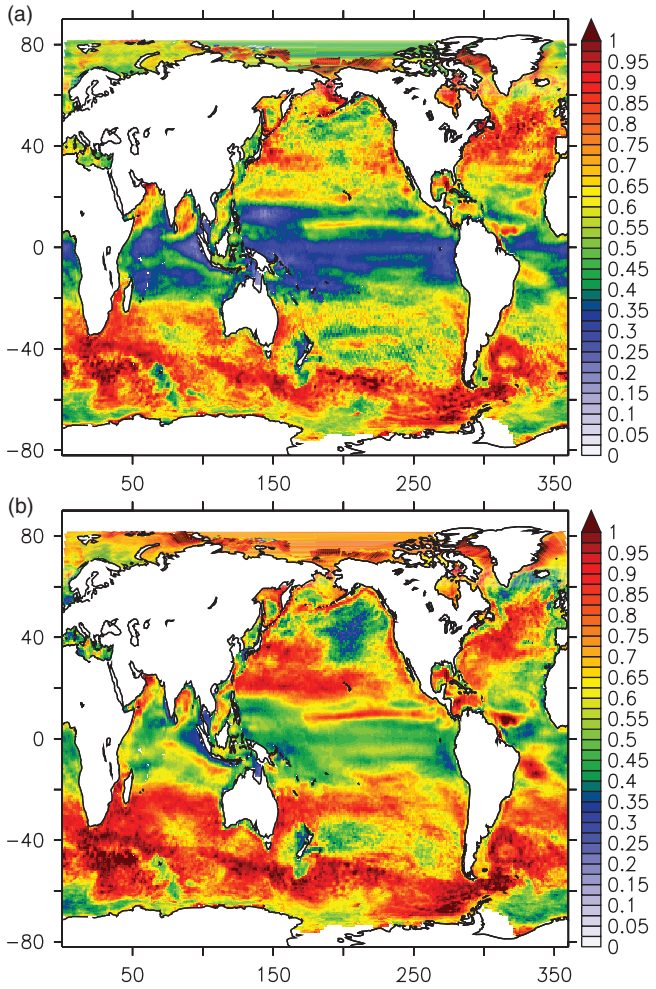

Figure 6. RMS difference from mapped AVISO altimeter data of monthly mean sea-level anomalies of (a) GECCO2 and (b) CTRL, calculated over the period 1993–2011 and normalized by the square root of the sum of the respective variances. A value of 1 corresponds to no skill.

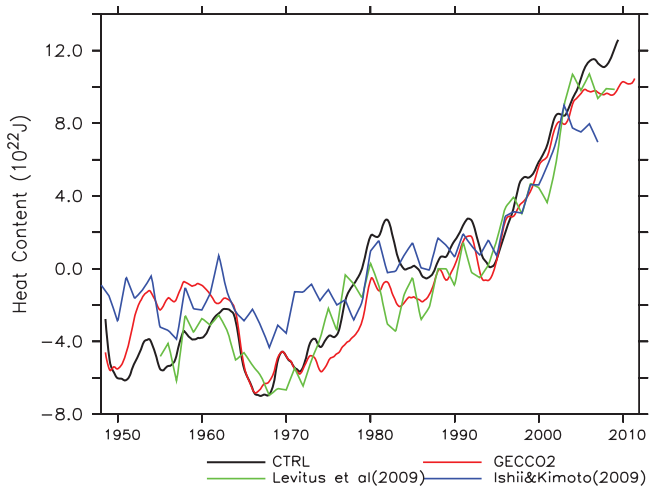

Figure 7. Global mean (0–700 m) heat content changes from CTRL and GECCO2 compared with estimates from Levitus *et al.* (2009) and Ishii and Kimoto (2009).

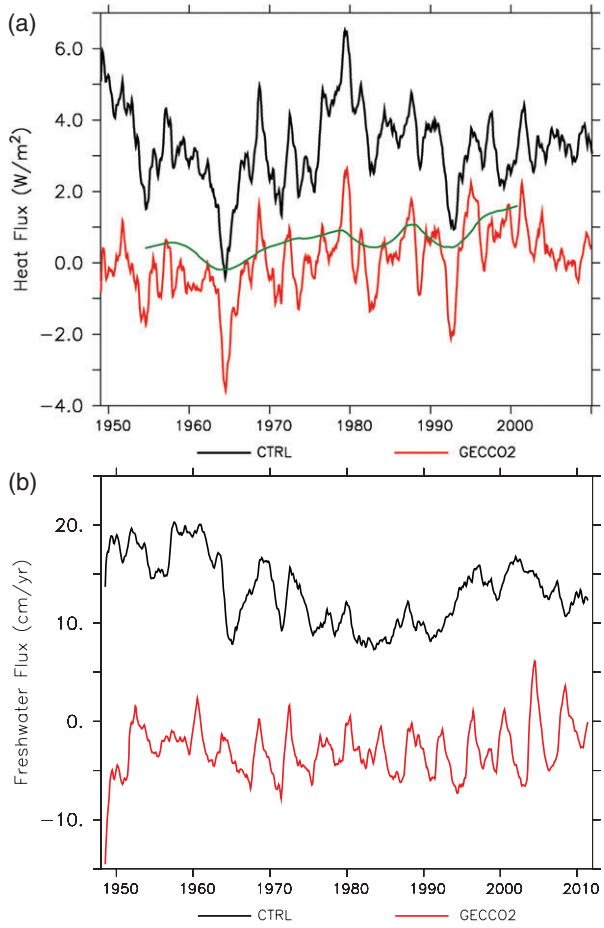

Figure 8. Global mean of (a) heat and (b) freshwater fluxes for GECCO2 and CTRL. (a) shows the radiation-based estimate of Murphy *et al.* (2009) (green), which appears smoother due to the application of an 8-year smoothing.

which describes an apparent overturning circulation which solely arises due to the depth dependence of the density surfaces and disappears if the overturning is calculated as function of density.

In isobaric coordinates, the maximum of the AMOC changes from below 15 Sv in CTRL to more than 18 Sv in GECCO2, while its location shifts northward from a broader range between 20°N and 35°N to a more localized region between 30°N and 38°N (Figure 9). Although not the most obvious choice, σ_3 surfaces were selected to provide a better resolution of the weakly stratified deep ocean. The stream function on σ_3 surfaces is shown only for layers deeper than 40 m because the low stratification in the upper 40 m over a wide σ_3 range causes substantial errors in calculation of the stream function of up to several Sv. Although not obviously noticeable for AMOC, these errors or alternative choices for density (e.g. σ_2 or neutral densities) totally mask the signal for heat transport shown in Figure 15. Additionally, due to its very different water masses, the circulation in the Mediterranean could not be properly represented and was removed from the analysis, which creates some artifacts near 40°N, where the maximum overturning appears to be lower than for the calculation along isobars and a spurious maximum appears at 35°N around $\sigma_3 = 40$. Overall, a deepening of the upper cell is visible throughout the entire Atlantic where its maximum value at 33°N changes from 2800 m in CTRL to 3300 m in GECCO2. The strength of the deep cell is unchanged, having a maximum value of 6 Sv in the range of the calculation of Ganachaud and Wunsch (2000). However, an intensification of the extension of the deep cell north of 40°N in GECCO2 is noticeable.

A comparison to the observation-based estimate from the RAPID array at 26.5°N is shown in Figure 10. In comparison to CTRL, the depth of the maximum is shifted downward in GECCO2 by about 300 m and the strength is increased by 4 Sv, now matching the RAPID estimate, which is only slightly shallower, fairly well. The deep branch of the AMOC, although enhanced in GECCO2, is still substantially (up to 6 Sv) too weak. Although a correction to a weaker and deeper maximum of the bottom cell is noticeable in GECCO2, in both simulations the cell is with a maximum of 4 Sv stronger than RAPID (2 Sv) and substantially shallower: 4000 m for CTRL and 4250 m for GECCO2 compared with 5200 m for RAPID.

Integrated along σ_3 surfaces, the overturning is denoted AMOCd in the following (Figure 9(c, d)). Compared with AMOC,

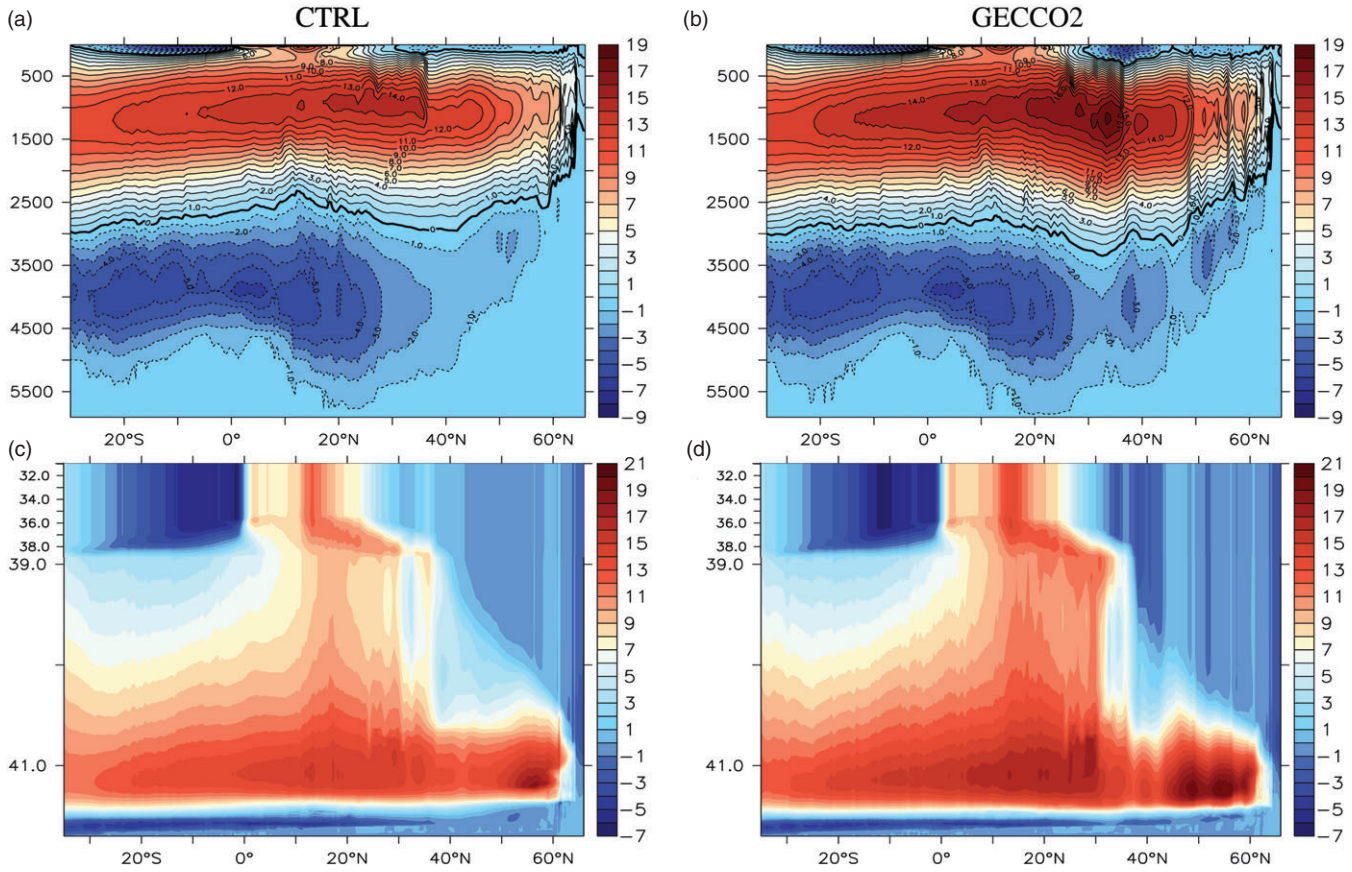

Figure 9. Mean (1948–2011) Atlantic meridional overturning stream function for (a, c) CTRL and (b, d) GECCO2 in physical space and zonally integrated along σ_3 surfaces.

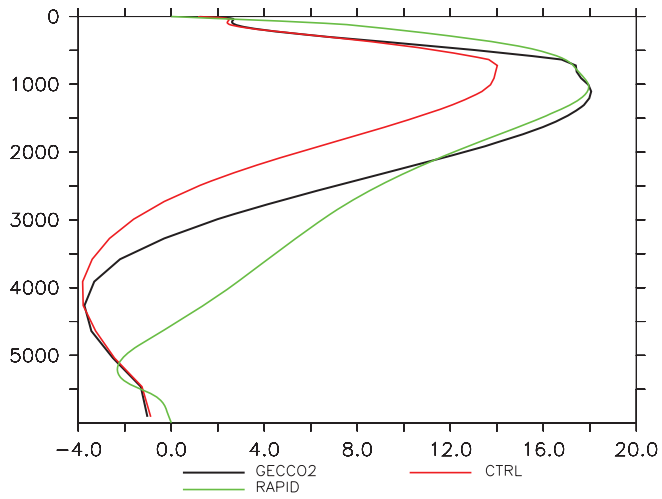

Figure 10. Vertical profile of the overturning transport (Sv) from CTRL, GECCO2 and RAPID.

the AMOCd maxima of GECCO2 and CTRL are shifted farther to the south and are now located near 20°N, where the maximum is slightly stronger in CTRL but about 1 Sv weaker in GECCO2 than the corresponding values of AMOC. The latter is related to the exclusion of the Mediterranean as its signal coincides with the maximum of the calculation over fixed depth levels. A second stronger maximum associated with the circulation and water mass transformation in the subpolar gyre appears north of 50°N. It appears as a single maximum in CTRL while in GECCO2 it is split into three cores, one located south of 50°N.

Analogous to Köhl and Stammer (2008b, their Figure 5a), we show in Figure 11 Hovmöller diagrams of the anomalies of maximum AMOC and AMOCd. As before, a close relation to the NAO exists and the estimates from GECCO and GECCO2 agree in showing a strengthening of the AMOC over the period 1950–2000, with more or less consistent maxima in the 1980s and 1990s. Although GECCO2 also shows propagation from the north towards the Equator, different from GECCO, no slow propagation north of 40°N is visible. Instead, the signal north of 50°N is much smaller and shows no correlation with the AMOC farther south (Figure 11(c)). If integrated along σ_3 surfaces, larger signals emerge north of 50°N, which appear to be correlated with the subtropical AMOCd. The correlation of the AMOCd at 25°N to the subpolar area is partly related to long-term changes and reduced to half after detrending. In density space, the overturning stream function shows the water mass transformation in the circulation of the subpolar gyre. The larger correlation in density space suggests that this transformation influences the AMOC farther south, while the origin of the anomalies that appear between 40°and 50°N remains unclear in the AMOC plot (Figure 11(a)).

Contributions to the lower, southward moving limb of the AMOC, the North Atlantic Deep Water (NADW), originate from the overflows over the Greenland–Iceland–Scotland Ridge and the water mass formation in the Labrador Sea (e.g. Schmitz and McCartney, 1993). Variability of the sources was suspected to impact the variability of the AMOC (e.g. Delworth *et al.*, 1993; Dickson *et al.*, 2002). While Köhl and Stammer (2008b) see in GECCO a dominant influence of the Denmark Strait overflow and only a minor contribution from the Labrador Sea, Böning *et al.* (2006) discuss only a relation between AMOC and the mixed-layer depth in the Labrador Sea.

Table 1 shows that the high correlation to the Denmark Strait overflow is a feature of GECCO but absent in CTRL and much reduced in GECCO2, where it appears mainly due to an increase in overflow strength during the 1990s (not shown). The difference impacts the structure of the AMOC. Downstream of the sill, the signal of the overflows soon reaches depths greater than 1000 m and therefore leaves an imprint on the AMOC. In GECCO2, the role of the Denmark Strait overflow is replaced by the importance

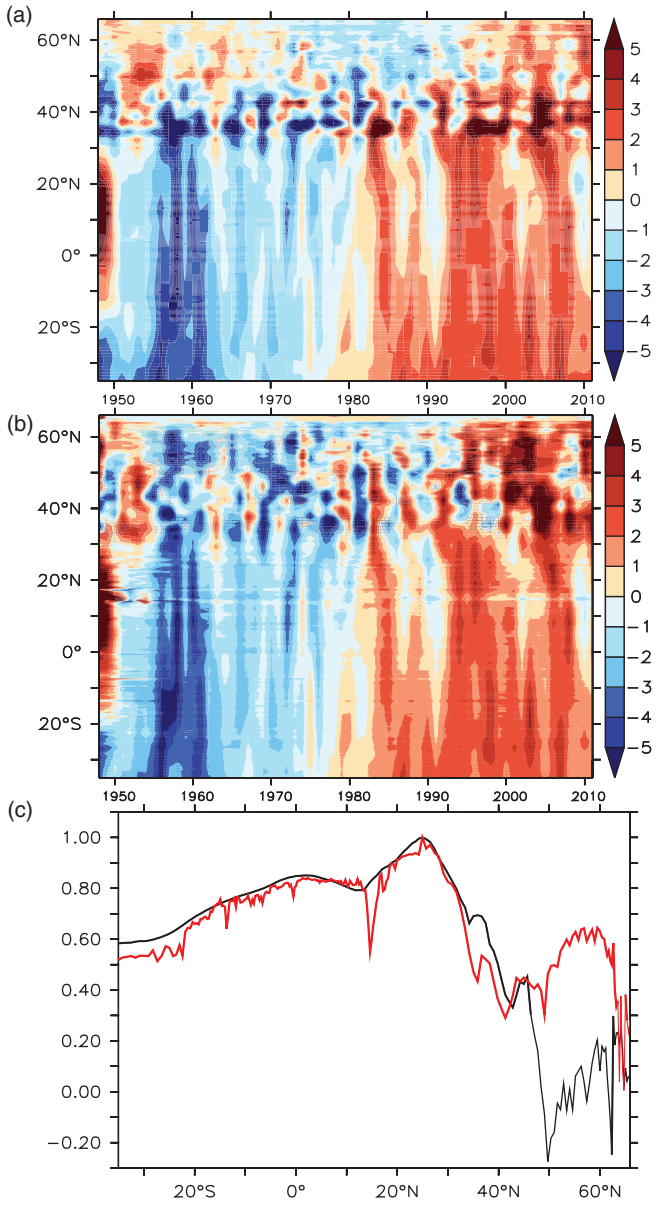

Figure 11. Anomalies of maximum AMOC or AMOCd (Sv) of GECCO2 calculated (a) in physical space and (b) along σ_3 surfaces. (c) Correlation of annual mean maximum AMOC at 25°N with the maximum AMOC at other latitudes if zonally integrated in physical space (black) or along density surfaces (red); correlations significant at the 95% level are shown in bold.

Table 1. Correlation coefficients C (with lags L in years) between the AMOC, the Denmark Strait overflow (DS), the stream function (Ψ) and the annual maximum of the maximum of the mixed layer depth (MLD) in the Labrador Sea (60–50°W, 54–60°N). Correlations are based on annual means, except for DS which is based on monthly data filtered with a 12-month running mean to be consistent with Köhl and Stammer (2008b). The correlation with the stream function is taken as the minimum in the area 60–50°W, 54–60°N.

	GECCO2	GECCO	CTRL
$C_{\mathrm{AMOC(48N),DS}}$	0.34	0.83	0.04
$L_{\mathrm{AMOC(48N),DS}}$	4.5	5.5	1.5
$C_{\mathrm{AMOC(55N),\Psi}}$	−0.23	−0.76	−0.74
$C_{\mathrm{AMOCd(55N),\Psi}}$	−0.83	−0.94	−0.77
$C_{\mathrm{MLD},\Psi}$	−0.7	−0.53	−0.55
$L_{\mathrm{MLD},\Psi}$	0	1	1

of the variability of the water mass transformation in the subpolar gyre. This signal remains shallow at first and descends to greater depth only south of about 50°S.

Correspondingly, Figure 12 shows that only AMOCd at 55°N is highly correlated with the circulation strength of the subpolar gyre, while the correlation to AMOC is much smaller (Table 1).

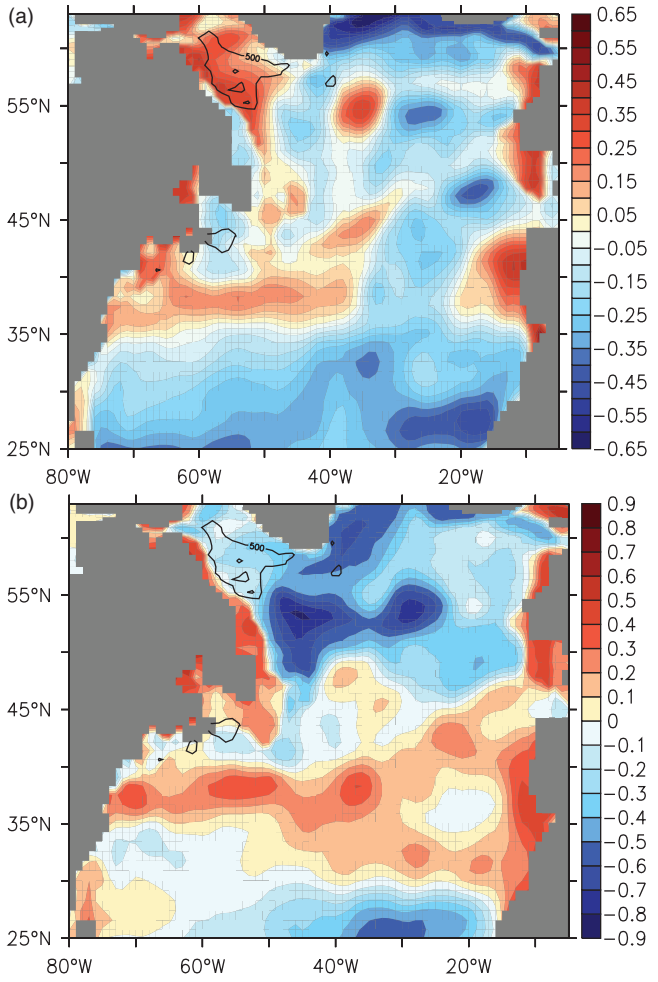

Figure 12. Correlation of the annual mean maximum AMOC at 55°N with the annual mean barotropic stream function in the North Atlantic for (a) AMOC and (b) AMOCd. Overlayed as black contours are the STD of the annual maximum mixed-layer depth (m), indicating the convection region.

Both show high correlation in the Irminger Sea, which indicates a relation to the overflow through the Denmark Strait. For AMOCd, the pattern of correlation basically shows which part of the stream function corresponds to the variance of the thermohaline circulation that is related to changes of the gyre circulation. The relation to the circulation in the Labrador Sea becomes apparent, which additionally reveals the pathway of the gyre that contributes most to the variability of the flow that involves density transformation. For GECCO, the close relation of the AMOC to the overflow and its deeper impact on the AMOC leads to high correlation between the gyre strength and both AMOC and AMOCd. However, despite low correlation to the overflow, the CTRL AMOC shows a high correlation to the gyre strength.

With a lag of about 1 year, the gyre strength shows the maximum correlation to the mixed-layer depth in the centre of the Labrador Sea as reported earlier (Eden and Willebrand, 2001; Böning *et al.*, 2006). In GECCO2, the initial barotropic response to enhanced mixed-layer depths starts in the northwestern part of the Labrador Sea near the region of the maximum mixed-layer depth variability (Figure 12). During the following years, the response moves southwestward and once it involves the extension of the North Atlantic current, an overturning signal becomes noticeable in density space (for GECCO and CTRL also in AMOC). Instead of the slow propagation north of 48°N seen in GECCO, propagation speeds remain fast throughout the entire North Atlantic, but the lag between the gyre and the overturning response introduces a similar delay.

Noteworthy in Figure 12(b) is the clear dipole structure east of the Labrador shelf break emphasizing the importance of the along-shelf current system for the AMOC farther south.

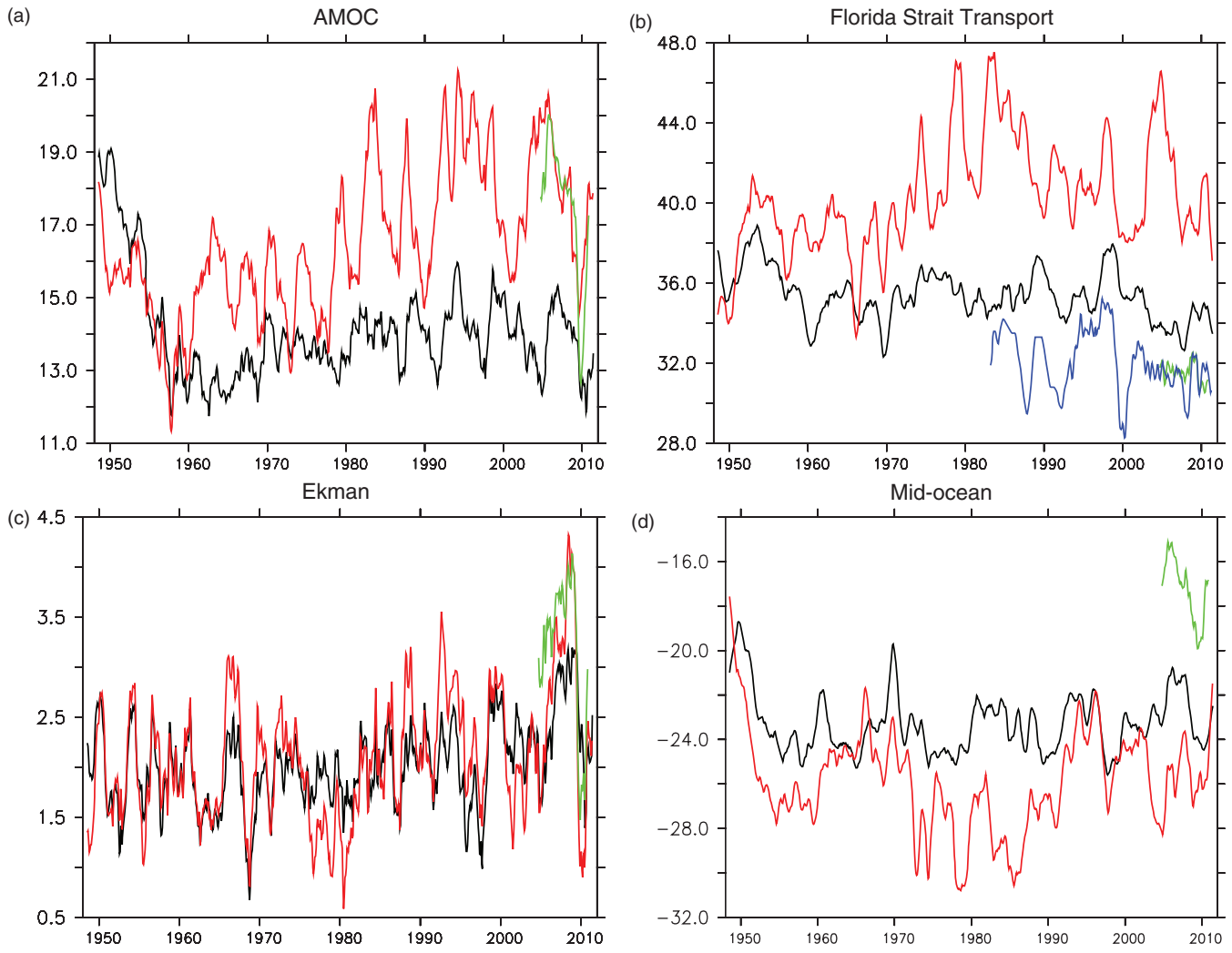

Figure 13. Comparison of the annual mean transports (Sv) from GECCO2 (red) and CTRL (black) with data from RAPID (green) and cable measurements (blue) for (a) the AMOC, (b) the Florida Strait, (c) the Ekman, and (d) the mid-ocean transports.

This region has long been the focus of observational studies (Fischer *et al.*, 2010). Their study demonstrated no significant trend in the strength of the along-shore flow over the period 1997 to 2009 while the boundary current showed a decadal warming rate of the order of $0.05\,^{\circ}\mathrm{C\,yr^{-1}}$. GECCO2 shows the same warming rate as the observations (not shown) but a temperature bias at the depth of the Labrador Sea water. The bias is with 0.5 °C as large as the total change during the decade. In agreement with the observations, no overall trend of the gyre circulation is seen in GECCO2 and it should be noted that in GECCO2 similar warming trends appear also before the 1990s (not shown).

In order to facilitate a direct comparison to the RAPID observational estimates (Rayner *et al.*, 2011), the AMOC at 26.5°N is decomposed into the contributions from the Florida Strait, the Ekman part and the upper mid-ocean transport. Figure 13 shows the complete time series as annual means. Superimposed as shorter time series, the RAPID estimates and estimates from cable measurements (http://www.aoml.noaa.gov/phod/floridacurrent/) are shown. Compared with CTRL, the GECCO2 AMOC mean value and the variability is substantially higher (16.6 Sv and 3.3 Sv in comparison to 14.1 Sv and 2.5 Sv), and the location of the minima and maxima are changed ($r = 0.52$). GECCO2 is very close to RAPID, although the minimum in 2009 is not quite as low. However, substantial differences for the Florida Strait transport (FST) exist in comparison to the cable measurements, particularly in terms of the strength of the signal, which is much too strong (40.2 Sv). Here, CTRL is in better agreement, particularly after 2000 when the NCEP can profit from the availability of QuikSCAT scatterometer wind data.

Since AMOC and Ekman transport agree well with RAPID, the too large FST has to be balanced by an also too large mid-ocean transport. The reason for this deficiency is that the model does not show an Antilles Current and the associated transport, which could range from 6 Sv (Meinen *et al.*, 2004) to 12 Sv (Schmitz and McCartney, 1993), appears as part of the FST. This explains the too large mid-ocean transport which, in the model, therefore corresponds to just the southward part of the mid-ocean transport of RAPID. Consequently, the difference model FST minus RAPID FST could be interpreted as the transport of the Antilles Current. In fact, if this difference is added to the mid-ocean transport of GECCO2, its difference from RAPID is reduced to less than 1 Sv, and the correlation improves ($r = 0.61$). A potential cause could be that the model does not resolve the topography, and the Bahamas Banks are realized as an island. Since the Antilles Current is also missing in CTRL, its better agreement with the observed Florida Strait transport points to too low a gyre strength. The difference between GECCO2 and CTRL can be attributed to the adjustments in wind. Applying the Sverdrup relation to the changes in wind stress curl yields a larger transport for GECCO2 by 4.8 Sv, which is close to the differences in FCT, although the wind changes appear to be small along 26.5°N (Figure 2).

For the period 2004–2011, the decomposition is shown as monthly means in Figure 14. Over this period, the mean and STD of GECCO2's AMOC matches those of RAPID (18.1 Sv and 3.5 Sv versus 17.4 Sv and 3.9 Sv, respectively, with $r = 0.75$), while CTRL (13.7 Sv and 2.5 Sv with $r = 0.68$) has much smaller values.

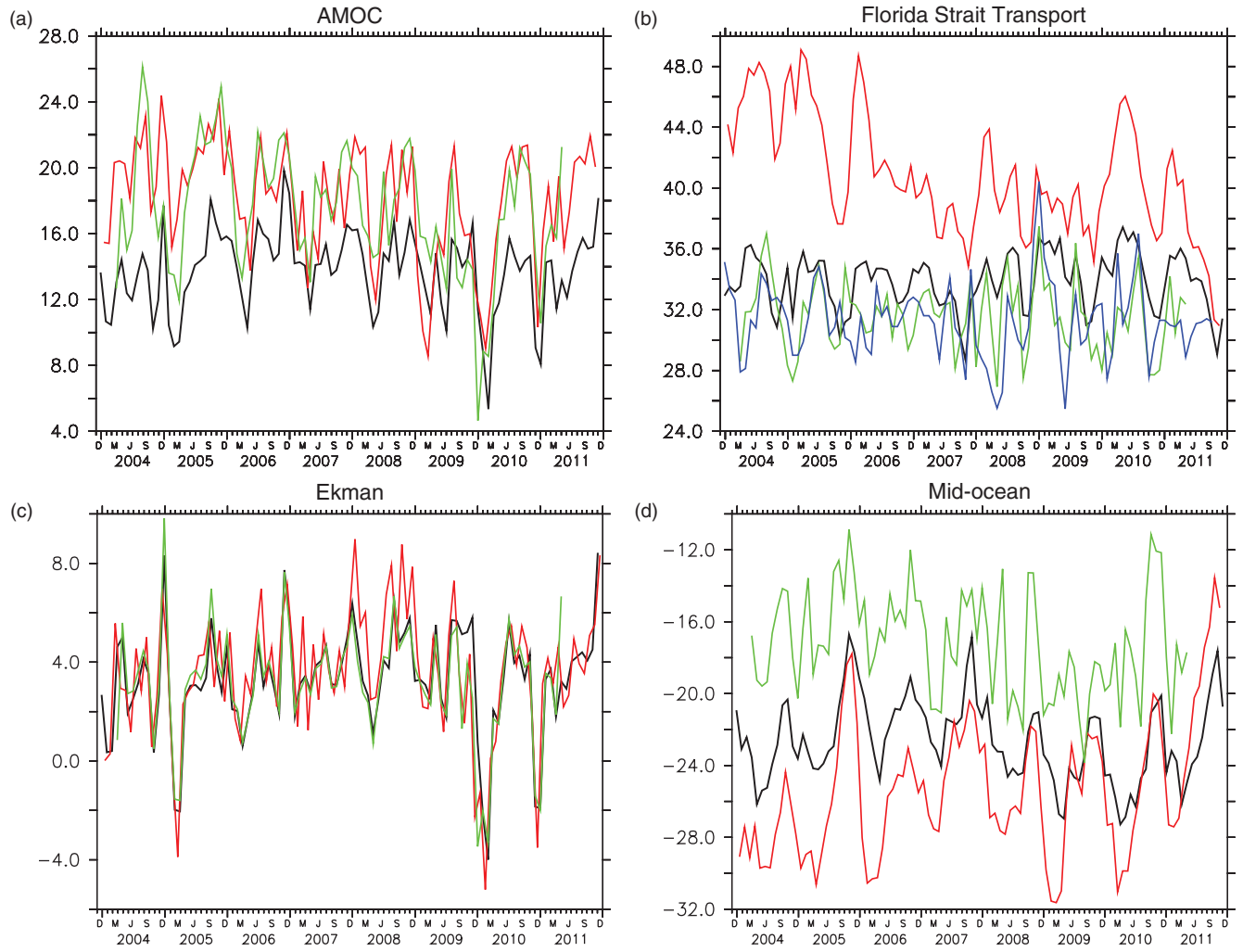

Figure 14. Comparison of the monthly mean transports (Sv) for the period 2005–2011 from GECCO2 (red) and CTRL (black) with data from RAPID (green) and cable measurements (blue) for (a) the AMOC, (b) the Florida Strait, (c) the Ekman, and (d) the mid-ocean transports.

As explained above, the FST is much too strong in GECCO2 and does not correspond to the observations ($r = 0.30$), while CTRL is only 2 Sv too strong and shows a somewhat better correlation ($r = 0.40$). Ekman transports correspond well. In GECCO2 and CTRL, the mid-ocean transport shows a clear seasonal cycle, which is almost unnoticeable in RAPID due to superimposed higher-frequency oscillation. This is likely due to eddy variability which the model does not resolve. Accordingly, a harmonic analysis (not shown) shows a good agreement in amplitude (2.5 Sv) and phase (minimum transport in October) across all three estimates.

4.3. *Heat transports*

According to Vonder Haar and Oort (1973) the ocean contributes about 50% to the maximum meridional heat transport (MHT) in the Northern Hemisphere. However, their total of close to 4 PW was more recently re-evaluated, and Trenberth and Caron (2001) report a larger value of 5.0 PW. The oceanic contribution to the total is largest at around 20°N and was estimated to be 2.5 PW, while Trenberth and Caron (2001) report a range of 1.5 to 2.0 PW from atmospheric reanalyzes. Section-based estimates exist sightly further north at 24°N, essentially spanning the same range (Ganachaud and Wunsch, 2000; Trenberth and Caron, 2001; Bryden and Imawaki, 2001, and references therein). The maximum poleward MHT of GECCO2 amounts to 1.93 PW and 1.6 PW in the Northern and Southern Hemisphere, respectively, and is therefore considerably larger than the previous estimate based on ECCO by Stammer *et al.* (2004) (1.7 PW and 0.7 PW, respectively). In the Southern Hemisphere, there is considerable uncertainty of the poleward MHT with maximum values between 0.5 and more than 2 PW (Ganachaud and Wunsch, 2000).

In the North Atlantic, the maximum MHT exists between 14°N and 24°N and its value ranges between 1.2 and 1.3 PW (Bryden and Imawaki, 2001; Lumpkin and Speer, 2007), which is consistent with a maximum of 1.1 PW of GECCO2 shown in Figure 15, while for CTRL it is 0.2 PW lower. For the period April 2004 to October 2007, an estimate of 1.35 PW exists at 26.5°N from the RAPID array (Johns *et al.*, 2011). In GECCO2, this would be a higher estimate due to the positive AMOC trend and a maximum MHT in summer. However, because values at 26.5°N are lower than the maximum, GECCO2 again yields for this period 1.1 PW.

Traditionally, in order to distinguish transports associated with the gyre circulation from those related to the thermohaline circulation, the variables are split into their zonal mean and the deviation (Bryan, 1982):

$$v = \langle v \rangle + v', \qquad T = \langle T \rangle + T'. \tag{1}$$

The heat transport can then be separated into the component due to the zonal mean and the deviation from the zonal mean,

$$H(y) = H_{\mathrm{OT}} + H_{\mathrm{GY}} \tag{2}$$

$$= \rho_o c_p \int_{-\mathcal{H}}^{0} \int_{x_{\mathrm{W}}}^{x_{\mathrm{E}}} \left(\langle v \rangle \langle T \rangle + v' T' \right) \mathrm{d}x\mathrm{d}z\,, \tag{3}$$

which, with the reference density ρ_0 and the specific heat capacity c_p, define the overturning (H_{OT}) and gyre (H_{GY}) components of the heat transport.

However, one has to keep in mind that the decomposition into overturning and gyre components is only a formal one and, even without any gyre circulation, a zonal temperature gradient would already produce a gyre component if, for example, the overturning is concentrated at the western boundary. Therefore, the decomposition is most problematic in cases of large zonal temperature gradients, as is the case for the subpolar gyre. As we have seen above, the thermohaline circulation should be described in density coordinates, because its characteristic is the transformation of density rather than a change in depth. Moreover, because the temperature gradient on density surfaces is much smaller, the alternative definition reduces the problem associated with temperature gradients and provides a more physically relevant decomposition.

Analogous to the definition of the overturning in density coordinates, the decomposition is extended to the integration on density surfaces, and the zonal mean is defined on the density surface $z(\sigma, x, y)$ with $L(y, \sigma)$ the length of the integration path as

$$\langle v \rangle_\sigma = \frac{1}{L(y,\sigma)} \int_{x_W}^{x_E} v\{x, y, z(\sigma, x, y)\}\, \mathrm{d}x. \tag{4}$$

By replacing the integration along isobars and over depth by the integration along isopycnals and over density,

$$H = H^\sigma_{\mathrm{OT}} + H^\sigma_{\mathrm{GY}} \tag{5}$$

$$= \rho_o c_p \int_{\sigma_{\max}}^{\sigma_{\min}} \int_{x_W}^{x_E} \left(\langle v \rangle_\sigma \langle T \rangle_\sigma + v'_\sigma T'_\sigma \right) \frac{\partial z}{\partial \sigma}\, \mathrm{d}x \mathrm{d}\sigma, \tag{6}$$

the overturning (H^σ_{OT}) and the gyre component (H^σ_{GY}) are defined, in which $\partial z/\partial\sigma$ describes the layer thickness and v'_σ the deviation from the zonal mean. Heat and freshwater fluxes lead to changes of water mass properties and their transport results in the transport of heat and freshwater. Therefore, the expectation is that transports of heat and freshwater are carried by the thermohaline circulation rather than by the gyre circulation. The objective here is to test the hypothesis that transports are mainly associated with the thermohaline circulation, while interpretations based on the traditional decomposition are obscured by spurious components due to changes in isopycnal height.

In the midlatitudinal North Atlantic, the meridional heat transport is tightly connected with the AMOC (e.g. Wunsch, 1980; Roemmich and Wunsch, 1985) while modelling results suggest that, in the subpolar gyre due to the large zonal temperature gradient, the gyre circulation becomes more important (Dong and Sutton, 2002). Figure 15 shows the decomposition into the overturning and gyre components of the heat transport. Consistent with Dong and Sutton (2002), the gyre component (unless otherwise noted we refer to the components in physical space in the following) explains close to 90% of the total MHT in the subpolar gyre at 55°N. However, despite their argument but consistent with their Figure 3, the subpolar gyre is not the only place with a significant contribution from the gyre component.

Near 30°N and in the equatorial region south of the Equator, the contribution from the gyre component reaches 0.2 PW. In the latter case, it accounts for about half of the total while at 30°N, the contribution is just 20% of the total. At 25°N, in agreement with previous results, it is only a few percent. The origin is evident; much of the warm northward transport is carried by the Gulf Stream. Since the associated volume transport is larger than the volume transport of the AMOC, the temperature of return flow in the upper ocean determines the barotropic component. A substantial fraction of the return flow takes place on the east side of the basin as the Canary Current and in the Cape Verde Frontal Zone. As directed southward and because of the entrained upwelled water from the coast, the associated currents are relatively cold. Although the Canary Current carries only about 2 Sv between the Canary Islands and Africa (Hernández-Guerra

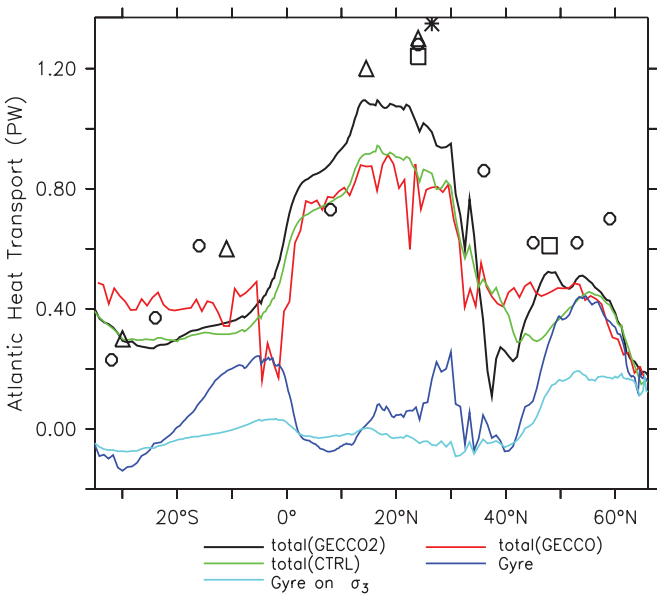

Figure 15. Heat transport in the Atlantic Ocean for GECCO2 as total and as decomposed into its gyre and overturning components. The decomposition is done is physical space as well as along σ_3 surfaces. The total fluxes are also shown for CTRL and GECCO. The overturning components can be easily retrieved from the difference between the total and the gyre components, and are not shown to improve clarity. Triangles, squares, circles and the asterisk denote the estimates from Bryden and Imawaki (2001), Lumpkin and Speer (2007), Talley (2003) and Johns *et al.* (2011), respectively.

et al., 2002), the total transport between 35°W and the African coast is estimated to be 11 Sv (Stramma, 1984). In GECCO2, the transport between 35°W and the African coast is 15 Sv larger.

A different situation exist south of the Equator. Here, the same calculation reveals that only about 50% of the gyre heat transport can be attributed to gyre circulation, while the rest remains concentrated in the western boundary. Accordingly at 8°S, the correlations between the gyre and the overturning component is positive and high ($r = 0.73$), while at 30°N it remains low and negative ($r = -0.33$). In the Southern Hemisphere, the Angola Current takes the role of the Canary Current. Beneath the warm tropical surface water layer, the larger-scale cyclonic Angola Gyre transports relatively cold water on its eastern side towards the south. Although much warmer than the northward flowing Benguela Current (Stramma and Schott, 1999), with temperature below 20 °C at 100 m it is about 10 °C colder than the northward flowing Brazil Current on the western side of the basin. In GECCO2, the current transports only 1.7 Sv across the distance from the centre of the gyre to the African coast, larger than the estimate of 1 Sv by Lass *et al.* (2000), while the estimate by Gordon and Bosley (1991) of 5 Sv may lead to much larger a contribution to the heat transport.

Along density surfaces, the gyre component disappears except for the subpolar gyre region, where little more than one third remains. This indicates, as suspected above, that much of the heat transport attributed to the gyre circulation is in fact also thermohaline in nature. As the water mass transformation in the subpolar gyre contributes to the overturning in density space, the associated heat transport largely shows up as overturning heat transport on density surfaces. In the subtropics, the circulation in the shallow subtropical overturning cells represents an important contribution to the heat transport. The circulation is characterized by the spreading of warm water in the western boundary currents which experience buoyancy loss. This water returns in part as mode water which gets subducted below less dense water in the return flow towards the Equator (Talley, 1999). In agreement with this picture, the disappearance of the gyre component on density surfaces demonstrates that the subtropical cells are essentially part of a thermohaline circulation, although they also involve the gyre circulation (as the discussion above shows).

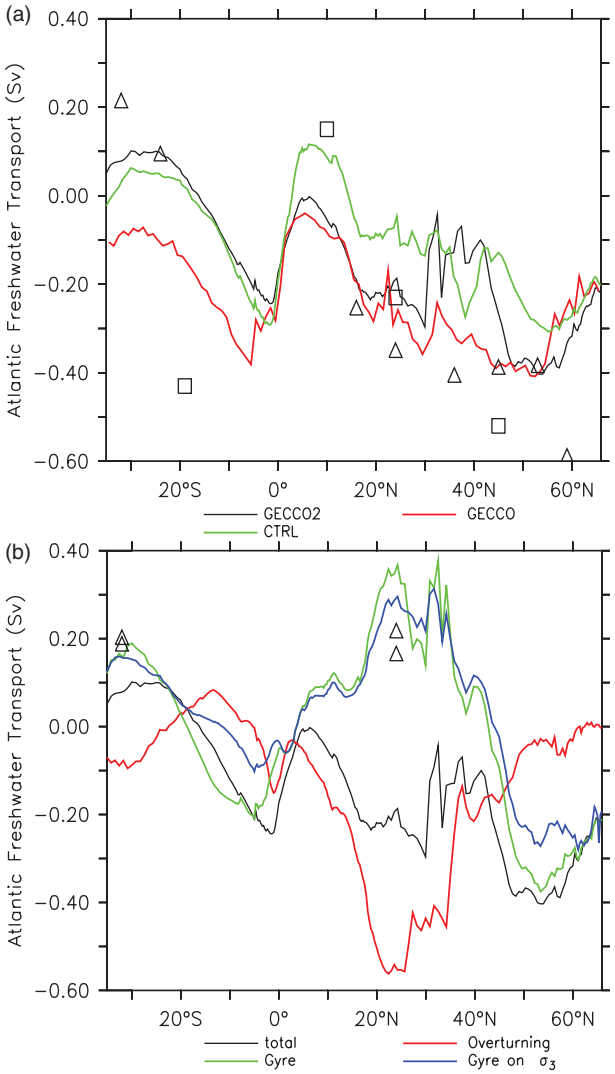

Figure 16. (a) Atlantic freshwater transports for GECCO2, CTRL and GECCO with estimates from Wijffels *et al.* (2001) and Talley (2008) superimposed as squares and triangles, respectively. (b) shows the total and the decomposition into gyre and overturning components. Triangles denote the estimates from the mass-balanced shallow overturning gyre by Talley (2008). The decomposition is done is physical space as well as along σ_3 surfaces. For the latter, we show only the gyre component.

4.4. *Freshwater transports*

Estimates of meridional transports of freshwater are traditionally based on either atmospheric data (Béranger *et al.*, 1999; Trenberth and Dai, 2003), box inverse methods (Ganachaud and Wunsch, 2000; Wijffels *et al.*, 2001) or absolute geostrophic transports (Talley, 2008). An alternative is provided here from the ocean freshwater transports of the GECCO2 synthesis. In comparison to the previous estimates based on the ECCO (Stammer *et al.*, 2004) and the GECCO (Romanova *et al.*, 2010) syntheses, the global freshwater transport of GECCO2 is very similar, except that the northward freshwater flux between about 5°N and 15°N is much smaller, barely reaching 0.03 Sv (not shown). In the North Atlantic, GECCO2 shows an inflow of 0.22 Sv from the Arctic which GECCO previously could not represent due to its closed boundaries at 80°N (Figure 16; note that the transports of GECCO were adjusted to match GECCO2 at 65°N and that, without the adjustment, GECCO more closely follows CTRL). The export from the Arctic is much lower than the 0.591 Sv reported by Talley (2008) for 59°N but quite close to the estimate of 0.245 Sv by Rudels *et al.* (2008). Despite the large export from the Arctic, in GECCO2 the Atlantic still imports freshwater at the southern border. Both GECCO (after correction) and GECCO2 are in much better agreement with the estimates collected by Wijffels *et al.* (2001) and Talley (2008), except for 10°N, where CTRL is closer.

As was done for the heat transport, the freshwater transport is decomposed into overturning and gyre components for the integration along isobaric as well as along σ_3 surfaces. In the Northern Hemisphere, the southward transport of freshwater is carried by the overturning component due to the DWBC carrying relatively fresh North Atlantic Deep Water in comparison to the saline North Atlantic Current. This component is described by (Talley, 2008) as part of the thermohaline circulation. However, in the subtropical gyre, as noted by Rahmstorf (1996), the gyre component is northward and renders the total southward transport to be less than half of the overturning part. He concluded that the northward gyre transport would have to balance not only the evaporation in the subtropical gyre but also the southward transport through the overturning component. However, the divergence of the transports matters for the balance of freshwater loss through the surface while the transport itself balances the other transport component. Therefore, it is convergence caused by the decrease (towards the Equator) of the southward total (as opposed to the gyre component) which balances the freshwater loss in the subtropical gyre. North of 25°N, the source of the convergence is the gyre component, and south of 25°N it is the overturning component, while the convergences are reduced in each case by the divergences of the other components. Although these divergences and convergences give rise to changes of the transport with latitude, causal relations between the components cannot be inferred.

The reason for the large opposing components is that the western boundary current transports tropical water to the north and the part that recirculates gains salinity. The highest salinities of the world ocean are found in the Canary Current (Tomczak and Godfrey, 2003). This highlights the importance of the gyre circulation in the freshwater balance of the North Atlantic. At 24°N, the gyre component can be compared to the shallow overturning gyre estimate by Talley (2008) because at this location, as is also stated there, the transport is largely due to the nearly horizontal circulation at densities lower than 26.0 kg m^{-3}. This is confirmed by the small difference between the gyre and the gyre component calculated on σ_3 surfaces. However, since GECCO2 includes the whole water column, its transport at more than 0.35 Sv is substantially larger than found by Talley (2008). The situation changes in the subpolar gyre, where the gyre component carries more than 90% of the northward transport. Here, about one third of the freshwater transport in the gyre circulation is associated with the thermohaline circulation.

In midlatitudes, the compensation between gyre and overturning component does not only hold for the mean but also for the interannual variability ($r = -0.7$ to -0.8). However, the total freshwater transport follows the overturning component ($r = 0.7$) and shows very low correlation with the gyre component.

In the Southern Hemisphere, the total remains southward until close to 18°S and follows the gyre component as the overturning component is smaller than the gyre part. Also here in the subtropical gyre, overturning and gyre parts oppose each other. Until 15°S, the North Brazil Current in the west and the southward Angola Current at the eastern boundary determine the southward transport in the gyre part, while south of the Angola–Benguela Front the Brazil Current, including the southward Ekman transport and the northward Benguela Current, constitute the main shallow gyre circulation and its northward freshwater transport. The estimate agrees well with Talley (2008). The difference from the calculation on σ_3 surfaces shows that the southward gyre component is represented as overturning on density surfaces and therefore associated with subduction in the gyre.

Although small, the overturning component includes contributions from many different water masses. At 32°S, the transport

is southward, even though the relatively fresh Antarctic Bottom and Intermediate Water move northward and the saltier Brazil Current and North Atlantic Deep Water move southward; the northward moving Benguela Current, although relatively fresh in the near-surface gyre circulation, contributes to the southward freshwater transport, since it contributes to the NADW while being saltier than the NADW (Talley, 2008).

5. Conclusions

The main purpose of the article is the presentation and evaluation of the GECCO2 synthesis, firstly with assimilated data but also including independent data sources. The comparison with the previous GECCO synthesis as well as with the unconstrained run revealed that the better agreement of GECCO2 with the assimilated data is to a large extent related to improvements of the forward model. The higher vertical and horizontal resolution, particularly the forcing via the atmospheric state rather than fluxes, results in a better representation of the upper ocean. However, in the deep ocean below 2000 m larger differences from the data become noticeable. The estimated adjustments to the fluxes remain similar to GECCO, although also regional differences appear (e.g. in the Southern Ocean).

The assimilation of data does not necessarily lead to smaller model–data differences everywhere. Regionally, i.e. in the eastern North Pacific and North Atlantic, larger difference in the sea-level anomalies appear than for CTRL. Global heat content changes are in agreement with recent observational estimates (e.g. Domingues *et al.*, 2008; Levitus *et al.*, 2009; Ishii and Kimoto, 2009), and the estimate of the global heat flux is close to radiative forcing estimate by Murphy *et al.* (2009). Both show a clear effect of the radiative forcing from volcanic eruptions. A weak influence of ENSO as recently discussed by Balmaseda *et al.* (2013b) and Loeb *et al.* (2012) is visible outside the periods affected by volcanic eruptions. Unlike Balmaseda *et al.* (2013b), no contribution from the levels below 700 m to the warming is seen during the recent decade. However, the heat content changes in the deeper layers seem to be insufficiently constrained in GECCO2.

Although the most striking feature of GECCO2 is much the too strong Florida Strait transport, the agreement with the AMOC estimates of the RAPID array is very good in terms of mean, variability and correlation. The reason for the large transport is that the Antilles Current is redirected and enters the Caribbean and appears as part of the Florida Strait transport.

In contrast to GECCO, the importance of the Denmark Strait overflow for the variability of the AMOC is not seen in GECCO2. Instead, as previously noted (e.g. Böning *et al.*, 2006), the Labrador Sea convection and the associated spin-up of the subpolar gyre takes this role. In density coordinates, the water mass transformation in the subpolar gyre is revealed as part of the AMOC and therefore correlated with the AMOC variability further south.

Heat and freshwater transport estimates are largely consistent with previous estimates given that large uncertainties exist. The large export from the Arctic of 0.22 Sv is crucial for the improvement of GECCO2 over GECCO. The evaluation on density coordinates shows that the heat transport is largely carried by the thermohaline circulation. In the subpolar gyre, only about one third of the transport by the gyre remains in density coordinates. Except for the subpolar gyre, the total freshwater transport is a smaller residual of its opposing overturning and gyre components. Different from the heat transport, a substantial fraction of the freshwater transport is carried by the gyre circulation, a fact that changes only marginally and mainly in the Southern Hemisphere when evaluated along density surfaces. The reason is the close alignment of the density surfaces with the isotherms, which does not hold for the isohalines in the same way.

Although the northward salt transport by the overturning was identified to be the critical factor for the stability of AMOC (de Vries and Weber, 2005), variations of the gyre component at the southern boundary controlled the regime. Stable weak overturning states were found to be associated with southward export of freshwater by the overturning component. Since the GECCO2 estimate of the overturning component of the freshwater transport yields a southward export of about 0.1 Sv at 32°S, the application of the result of de Vries and Weber (2005) suggests that the current ocean state would facilitate a gradual reduction in AMOC as a smooth function of the added freshwater in the subpolar gyre as opposed to a rapid transition to low AMOC states. However, since the export may be a function of the overturning strength, this may change for larger freshwater perturbations.

Acknowledgements

This work was supported in the North Atlantic by the Bundesministerium für Bildung und Forschung (BMBF) projects RACE and MiKlip. The integration of the model simulations was performed at the German high-performance computing centre DKRZ with support from BMBF. Data from the RAPID-WATCH MOC monitoring project are funded by the Natural Environment Research Council and are freely available from http://www.noc.soton.ac.uk/rapidmoc. The Florida Current cable and section data are made freely available on the Atlantic Oceanographic and Meteorological Laboratory web page (http://www.aoml.noaa.gov/phod/floridacurrent/) and are funded by the NOAA Climate Observation Division. SSH maps were produced by Ssalto/Duacs as part of the Environment and Climate EU Enact project (EVK2-CT2001-00117) and distributed by Aviso, with support from CNES.

References

Bahurel P. 2006. Mercator ocean global to regional ocean monitoring and forecasting. *Ocean Weather Forecasting*, Chassignet EP, Verron J (eds.): 381–395. Springer: Berlin.

Balmaseda M, Alves O, Awaji T, Behringer D, Ferry N, Fujii Y, Lee T, Rienecker M, Rosati A, Smith D, Molteni F. 2010. 'Initialization for seasonal and decadal forecasts'. In *Proceedings of the OceanObs'09 Conference. 2: Community White Papers*, 21–25 September 2009. Venice, Italy, Hall J, Harrison DE, Stammer D. (eds.) ESA Publication WPP-306, doi: 10.5270/OceanObs09.

Balmaseda MA, Mogensen K, Weaver AT. 2013a. Evaluation of the ECMWF ocean reanalysis system ORAS4. *Q. J. R. Meteorol. Soc.* **139**: 1132–1161.

Balmaseda MA, Trenberth K, Källén W. 2013b. Distinctive climate signals in reanalysis of global ocean heat content. *Geophys. Res. Lett.* **40**: 1754–1759, doi: 10.1002/grl.50382.

Béranger K, Siefridt L, Barnier B, Garnier E, Roquet H. 1999. Evaluation of operational ECMWF surface freshwater fluxes over oceans during 1991–1997. *J. Mar. Syst.* **22**: 13–36.

Böning CW, Scheinert M, Dengg J, Biastoch A, Funk A. 2006. Decadal variability of the subpolar gyre transport and its reverberation in the North Atlantic overturning. *Geophys. Res. Lett.* **33**: L21S01, doi: 10.1029/2006GL026906.

Bryan K. 1982. Seasonal variation in meridional overturning and poleward heat transport in the Atlantic and Pacific Oceans: A model study. *J. Marine Res.* **40**: 39–53.

Bryan K. 1993. Ocean circulation models. In *Strategies for Future Climate Research*, Latif M. (ed.): 265–286. Max-Planck-Institute für Meteorologie: Hamburg, Germany.

Bryden HL, Imawaki S. 2001. Ocean circulation and climate: Observing and modelling the global ocean. In *Ocean Heat Transport*, Siedler G, Church J. (eds.): 455–474. Academic Press: London.

Carton JA, Santorelli A. 2008. Global decadal upper-ocean heat content as viewed in nine analyses. *J. Clim.* **21**: 6015–6035.

Delworth T, Manabe S, Stouffer RJ. 1993. Interdecadel variations of the thermohaline circulation in a coupled ocean-atmosphere model. *J. Clim.* **6**: 1993–2011.

Dickson B, Yashayaev I, Meincke J, Turrell B. 2002. Rapid freshening of the deep North Atlantic Ocean over the past four decades. *Nature* **416**: 832–836.

Domingues C, Church J, White N, Gleckler P, Wijffels S, Barker P, Dunn J. 2008. Improved estimates of upper-ocean warming and multi-decadal sea-level rise. *Nature* **453**: 1090–1093.

Dong B, Sutton R. 2002. Variability in North Atlantic heat content and heat transport in a coupled ocean–atmosphere GCM. *Clim. Dyn.* **19**: 485–497.

Dong B, Sutton RT. 2005. Mechanism of interdecadal thermohaline circulation variability in a coupled ocean-atmosphere GCM. *J. Clim.* **18**: 1117–1135.
Eden C, Willebrand J. 2001. Mechanism of interannual to decadal variability of the North Atlantic circulation. *J. Clim.* **14**: 2266–2280.
Fischer J, Visbeck M, Zantopp R, Nunes N. 2010. Interannual to decadal variability of outflow from the Labrador Sea. *Geophys. Res. Lett.* **37**: L24610, doi: 10.1029/2010GL045321.
Ganachaud A, Wunsch C. 2000. Improved estimates of global ocean circulation, heat transport, and mixing from hydrographic data. *Nature* **408**: 453–457.
Goddard L, Mason SJ, Zebiak SE, Ropelewski CF, Basher R, Cane MA. 2001. Current approaches to seasonal to interannual climate predictions. *Int. J. Climatol.* **21**: 1111–1152.
Gordon A, Bosley K. 1991. Cyclonic gyre in the tropical South Atlantic. *Deep-Sea Res. Part A* **38**: S323–S343.
Gouretski V, Koltermann KP. 2007. How much is the ocean really warming? *Geophys. Res. Lett.* **34**: L01610, doi: 10.1029/2006GL027834.
Gouretski V, Reseghetti F. 2010. On depth and temperature biases in bathythermograph data: Development of a new correction scheme based on analysis of a global ocean database. *Deep-Sea Res. I* **57**: 812–833, doi: 10.1016/j.dsr.2010.03.011.
Heimbach P, Forget G, Ponte R, Wunsch C, Balmaseda M, Awaji T, Baehr J, Behringer D, Carton J, Ferry N, Fischer A, Fukumori I, Giese B, Haines K, Harrison E, Hernandez F, Kamachi M, Keppenne C, Köhl A, Lee T, Menemenlis D, Oke P, Remy E, Rienecker M, Rosati A, Smith D, Speer K, Stammer D, Weaver A. 2010. 'Observational requirements for global-scale ocean climate analysis: Lessons from ocean state estimation'. In *Proceedings of the OceanObs'09 Conference 2*, September 2009. Venice, Italy, Hall J, Harrison DE, Stammer D. (eds.) ESA Publication WPP-306.
Hernández-Guerra A, Machin F, Antoranz A, Cisneros-Aguirre J, Gordo C, Marrero-Diaz A, Martinez A, Ratsimandresy A, Rodriguez-Santana A, Sangrá P, *et al.* 2002. Temporal variability of mass transport in the Canary Current. *Deep-Sea Res. II* **49**: 3415–3426.
Ingleby B, Huddleston M. 2007. Quality control of ocean temperature and salinity profiles –historical and real-time data. *J. Marine Syst.* **65**: 158–175.
Ishii M, Kimoto M. 2009. Re-evaluation of historical ocean heat content variations with time-varying XBT and MBT depth bias corrections. *J. Oceanogr.* **65**: 287–299, doi: 10.1007/s10872-009-0027-7.
Johns W, Baringer M, Beal L, Cunningham S, Kanzow T, Bryden HL, Hirschi J, Marotzke J, Meinen C, Shaw B, Curry R. 2011. Continuous, array-based estimates of Atlantic Ocean heat transport at 26.5°N. *J. Clim.* **24**: 2429–2449.
Keenlyside N, Latif M, Jungclaus J, Kornblueh L, Roeckner E. 2008. Advancing decadal-scale climate prediction in the North Atlantic sector. *Nature* **453**: 84–88.
Köhl A. 2014. Detecting processes contributing to interannual halosteric and thermosteric sea-level variability. *J. Clim.* **27**: 2417–2426, doi: 10.1175/JCLI-D-13-00412.1.
Köhl A, Stammer D. 2008a. Decadal sea level changes in the 50-year GECCO ocean synthesis. *J. Clim.* **38**: 1876–1890.
Köhl A, Stammer D. 2008b. Variability of the meridional overturning in the North Atlantic from the 50-year GECCO state estimation. *J. Phys. Oceanogr.* **38**: 1913–1930.
Köhl A, Dommenget D, Ueyoshi K, Stammer D. 2006. 'The global ECCO 1952 to 2001 ocean synthesis', ECCO report 40. http://www.ecco-group.org/pdfs/reports/report_40.pdf (accessed 23 February 2014).
Köhl A, Stammer D, Cornuelle B. 2007. Interannual to decadal changes in the ECCO global WOCE synthesis. *J. Phys. Oceanogr.* **37**: 313–337.
Köhl A, Siegismund F, Stammer D. 2012. Impact of assimilating bottom pressure anomalies from GRACE on ocean circulation estimates. *J. Geophys. Res.* **117**: C04032, doi: 10.1029/2011JC007623.
Kuhlbrodt T, Griesel A, Montoya M, Levermann A, Hofmann M, Rahmstorf S. 2007. On the driving processes of the Atlantic meridional overturning circulation. *Rev. Geophys.* **45**: RG2001, doi: 10.1029/2004RG000166.
Large WG, Pond S. 1981. Open ocean momentum flux measurements in moderate to strong winds. *J. Phys. Oceanogr.* **11**: 324–336.
Large WG, Pond S. 1982. Sensible and latent-heat flux measurements over the ocean. *J. Phys. Oceanogr.* **12**: 464–482.
Large WG, Yaeger SG. 2004. 'Diurnal to decadal global forcing for ocean and sea-ice models: The data sets and flux climatologies'. Technical Report TN-460+STR. NCAR: Boulder, CO.
Lass H, Schmidt M, Mohrholz V, Nausch G. 2000. Hydrographic and current measurements in the area of the Angola-Benguela front. *J. Phys. Oceanogr.* **30**: 2589–2609.
Lee T, Awaji T, Balmaseda M, Ferry N, Fujii Y, Fukumori I, Giese B, Heimbach P, Köhl A, Masina S, Remy E, Rosati A, Schodlok MP, Stammer D, Weaver AT. 2010a. Consistency and fidelity of Indonesian-throughflow total volume transport estimated by 14 ocean data assimilation products. *Dyn. Atmos Oceans* **50**: 201–223, doi: 10.1016/j.dynatmoce.2009.12.004.
Lee T, Stammer D, Awaji T, Balmaseda M, Behringer D, Carton J, Ferry N, Fischer A, Fukumori I, Giese B, Haines K, Harrison E, Heimbach P, Kamachi M, Keppenne C, Köhl A, Masina S, Menemenlis D, Ponte R, Remy E, Rienecker M, Rosati A, Schroeter J, Smith D, Weaver A, Wunsch C, Xue Y. 2010b. 'Ocean state estimation for climate research'. In *Proceedings of the OceanObs'09 Conference: 2*, 21–25 September 2009. Venice, Italy, Hall J, Harrison DE, Stammer D. (eds.) ESA Publication WPP-306.
Levitus S, Antonov JI, Boyer TP, Stephens C. 2000. Warming of the world ocean. *Science* **287**: 2225–2229.
Levitus S, Antonov J, Boyer T. 2005a. Warming of the world ocean. *Geophys. Res. Lett.* **32**: 1955–2003, doi: 10.1029/2004GL021791.
Levitus S, Antonov J, Boyer T, Garcia HE, Locarnini RA. 2005b. Linear trends of zonally averaged thermosteric, halosteric, and total steric sea level for individual ocean basins and the world ocean, (1955–59)–(1994–98). *Geophys. Res. Lett.* **32**: L16601, doi: 1029/2005GL023761.
Levitus S, Antonov J, Boyer T, Locarnini R, Garcia H, Mishonov A. 2009. Global ocean heat content 1955-2008 in light of recently revealed instrumentation problems. *Geophys. Res. Lett.* **36**: L07608, doi: 10.1029/2008GL037155.
Levitus S, Antonov J, Boyer T, Baranova O, Garcia H, Locarnini R, Mishonov A, Reagan J, Seidov D, Yarosh E, Zweng MM. 2012. World ocean heat content and thermosteric sea level change (0–2000 m). *Geophys. Res. Lett.* **39**: L10603, doi: 10.1029/2012GL051106.
Loeb NG, Lyman JM, Johnson GC, Allan RP, Doelling DR, Wong T, Soden BJ, Stephens GL. 2012. Observed changes in top-of-the-atmosphere radiation and upper-ocean heating consistent within uncertainty. *Nat. Geosci.* **5**: 110–113.
Lumpkin R, Speer K. 2007. Global ocean meridional overturning. *J. Phys. Oceanogr.* **37**: 2550–2562.
Marshall J, Schott F. 1999. Open-ocean convection: Observations, theory, and models. *Rev. Geophys. Res.* **37**: 1–64.
Marshall J, Hill C, Perelman L, Adcroft A. 1997. Hydrostatic, quasi-hydrostatic, and nonhydrostatic ocean modelling. *J. Geophys. Res.* **102**: 5733–5752, doi: 10.1029/96JC02776.
McCarthy JJ. 2001. *Climate Change 2001: Impacts, Adaptation, and Vulnerability: Contribution of Working Group II to the Third Assessment Report of the Intergovernmental Panel on Climate Change*. Cambridge University Press: Cambridge, UK.
Meinen CS, Garzoli SL, Johns WE, Baringer MO. 2004. Transport variability of the deep western boundary current and the Antilles Current off Abaco Island, Bahamas. *Deep-Sea Res. I* **51**: 1397–1415.
Munoz E, Kirtman B, Weijer W. 2011. Varied representation of the Atlantic meridional overturning across multidecadal ocean reanalyses. *Deep-Sea Res. II* **58**: 1848–1857.
Murphy D, Solomon S, Portmann RW, Rosenlof KH, Forster PM, Wong T. 2009. An observationally based energy balance for the earth since 1950. *J. Geophys. Res.* **114**: D17107, doi: 10.1029/2009JD012105.
Pail R, Goiginger H, Schuh W-D, Höck E, Brockmann J, Fecher T, Gruber T, Mayer-Gürr T, Kusche J, Jäggi A, Rieser D. 2010. Combined satellite gravity field model GOCO01S derived from GOCE and GRACE. *Geophys. Res. Lett.* **37**: L20314, doi: 10.1029/2010GL044906.
Pohlmann H, Jungclaus JH, Köhl A, Stammer D, Marotzke J. 2009. Initializing decadal climate predictions with the GECCO oceanic synthesis: Effects on the North Atlantic. *J. Clim.* **22**: 3926–3938.
Rahmstorf S. 1996. On the freshwater forcing and transport of the Atlantic thermohaline circulation. *Clim. Dyn.* **12**: 799–811.
Rayner D, Hirschi JJ-M, Kanzow T, Johns WE, Wright PG, Frajka-Williams E, Bryden HL, Meinen CS, Baringer MO, Marotzke J, Beal LM, Cunningham SA. 2011. Monitoring the Atlantic meridional overturning circulation. *Deep-Sea Res. II* **58**: 1744–1753.
Rintoul S, England M. 2002. Ekman transport dominates air–sea fluxes in driving variability of Subantarctic Mode Water. *J. Phys. Oceanogr.* **32**: 1308–1321.
Roemmich D, Gilson J. 2011. The global ocean imprint of ENSO. *Geophys. Res. Lett.* **38**: L13606, doi: 10.1029/2011GL047992.
Roemmich D, Wunsch C. 1985. Two Transatlantic sections: Meridional circulation and heat flux in the subtropical North Atlantic ocean. *Deep-Sea Res. A* **32**: 619–664.
Romanova V, Köhl A, Stammer D, Klepp AAC, Barkan S. 2010. Sea surface freshwater flux estimates from GECCO, HOAPS and NCEP. *Tellus* **62A**: 530–550, doi: 10.1111/j1600-0870.2010.00445.x.
Rudels B, Marnela M, Eriksson P. 2008. Constraints on estimating mass, heat and freshwater transports in the Arctic Ocean: An exercise. *Arctic-Subarctic Ocean Fluxes*, Dickson RR, Meincke J, Rhines P (eds.): 315–341. Springer: Berlin.
Schmitz WJ, McCartney WS. 1993. On the North Atlantic Circulation. *Rev. Geophys.* **31**: 29–49.
Smith DM, Cusack S, Colman AW, Folland CK, Harris GR, Murphy JM. 2007. Improved surface temperature prediction for the coming decade from a global climate model. *Science* **317**: 796–799.
Stammer D, Wunsch C, Giering R, Eckert C, Heimbach P, Marotzke J, Adcroft A, Hill C, Marshall J. 2002. The global ocean circulation during 1992–1997, estimated from ocean observations and a general circulation model. *J. Geophys. Res.* **107**: 1-1–1-27, doi: 10.1029/2001JC000888.
Stammer D, Ueyoshi K, Köhl A, Large WG, Josey SA, Wunsch C. 2004. Estimating air–sea fluxes of heat, freshwater, and momentum though global ocean data assimilation. *J. Geophys. Res.* **109**: C05023, doi: 10.1029/2003JC002082.
Stammer D, Köhl A, Awaji T, Carton MBDBJ, Ferry N, Fischer A, Fukumori I, Giese B, Haines K, Harrison E, Heimbach P, Kamachi M, Keppenne C, Lee T, Masina S, Menemenlis D, Ponte R, Remy E, Rienecker M, Rosati A, Schroeter J, Smith D, Weaver A, Wunsch C, Xue Y. 2010. 'Ocean information provided through ensemble ocean syntheses'. *Proceedings of the OceanObs'09 Conference: 2*, 21–25 September. Venice, Italy, Hall J, Harrison DE, Stammer D. (eds.) ESA Publication WPP-306, doi: 10.5270/OceanObs09.

Stramma L. 1984. Geostrophic transport in the warm water sphere of the eastern subtropical North Atlantic. *J. Marine Res.* **42**: 537–558.

Stramma L, Schott F. 1999. The mean flow field of the tropical Atlantic Ocean. *Deep-Sea Res. II* **46**: 279–303.

Sugiura N, Awaji T, Masuda S, Mochizuki T, Toyoda T, Miyama T, Igarashi H, Ishikawa Y. 2008. Development of a four-dimensional variational coupled data assimilation system for enhanced analysis and prediction of seasonal to interannual climate variations. *J. Geophys. Res.* **113**: C10, doi: 10.1029/2008JC004741.

Talley LD. 1999. Some aspects of ocean heat transport by the shallow, intermediate and deep overturning circulations. In *Mechanisms of Global Climate Change at Millennial Time Scales*, Clark PU, Webb RS, Keigwin LD. (eds.) *Geophysical Monograph*: 1–22. American Geophysical Union: Washington, DC, doi: 10.1029/GM112p0001.

Talley LD. 2003. Shallow, intermediate, and deep overturning components of the global heat budget. *J. Phys. Oceanogr.* **33**: 530–560.

Talley LD. 2008. Freshwater transport estimates and the global overturning circulation: shallow, deep and throughflow components. *Prog. Oceanogr.* **78**: 257–303.

Tomczak M, Godfrey JS. 2003. *Regional Oceanography: An Introduction*. Daya Books: New Delhi.

Trenberth KE, Caron JM. 2001. Estimates of meridional atmosphere and ocean heat transports. *J. Clim.* **14**: 3433–3443.

Trenberth KE, Dai A. 2003. New estimates of continental discharge and oceanic freshwater transport. *Proceedings of 7th International Conference on Southern Hemisphere Meteorology and Oceanography*, 24–28 March 2003, Wellington. American Meteorological Society: Boston, MA.

Vonder Haar TH, Oort AH. 1973. New estimate of annual poleward energy transport by northern hemisphere oceans. *J. Phys. Oceanogr.* **3**: 169–172.

de Vries P, Weber SL. 2005. The Atlantic freshwater budget as a diagnostic for the existence of a stable shut-down of the meridional overturning circulation. *Geophys. Res. Lett.* **32**: L09606, doi: 10.1029/2004GL021450.

Wijffels SE, Toole JM, Davis R. 2001. Revisiting the South Pacific subtropical circulation: A synthesis of World Ocean Circulation Experiment observations along 32°S. *J. Geophys. Res.* **106**: 19481–19513, doi: 10.1029/1999JC000118.

Wijffels SE, Willis J, Domingues CM, Barker P, White NJ, Gronell A, Ridgway K, Church JA. 2008. Changing expendable bathythermograph fall rates and their impact on estimates of thermosteric sea level rise. *J. Clim.* **21**: 5657–5672.

Wunsch C. 1980. Meridional heat flux of the North Atlantic Ocean. *Proc. Natl. Acad. Sci. U.S.A.* **77**: 5043–5047.

Wunsch C, Heimbach P. 2006. Decadal changes in the North Atlantic meridional overturning and heat flux. *J. Phys. Oceanogr.* **36**: 2012–2024.

Xue Y, Alves O, Balmaseda MA, Ferry N, Good S, Ishikawa I, Lee T, McPhaden MJ, Peterson KA, Rienecker M. 2010. 'Ocean state estimation for global ocean monitoring: ENSO and beyond ENSO'. In *Proceedings of the OceanObs'09 Conference: 2*, 21–25 September 2009. Venice, Italy. Hall J, Harrison DE, Stammer D. (eds.) ESA Publication: WPP-306, doi: 10.5270/OceanObs09.

Zhang JL, Rothrock D. 2000. Modeling Arctic sea ice with an efficient plastic solution. *J. Geophys. Res.* **105**: 3325–3338, doi: 10.1029/1999JC900320.

Zhang X, Sorteberg A, Zhang J, Gerdes R, Comiso JC. 2008. Recent radical shifts of atmospheric circulations and rapid changes in Arctic climate system. *Geophys. Res. Lett.* **35**: L22701, doi: 10.1029/2008GL035607.

